McMASTER UN

HAMILTON, ONTA

DEVELOPMENT OF NON-LEADED FREE MACHINING STEELS - PHASE IV

FINAL REPORT

April 1, 1984 - March 31, 1985

DEPARTMENT OF

AND MATERIA

DEVELOPMENT OF NON-LEADED FREE MACHINING STEELS - PHASE IV

FINAL REPORT

April 1, 1984 - March 31, 1985

S.V. Subramanian

and

D.A.R. Kay

Work on this project was conducted under the auspices of
Physical Metallurgy Research Laboratories
Canada Centre for Mineral and Energy Technology
Energy, Mines and Resources, Canada

DSS FILE NUMBER	:	13SV-23440-3-9134
DSS CONTRACT SERIAL NUMBER	:	OSV83-00048
CANMET PROJECT NUMBER	:	360251
CANMET SCIENTIFIC AUTHORITY	:	Mr. D.A. Parsons

This report should be cited by D.S.S.

File No. 13SV-23440-3-9134

MAR 3 1986

MICROMEDIA

67 pp

DARK-17a

FOREWORD

Phase IV of the project "Development of Non-Leaded Free Machining Steels" has been carried out in cooperation with Atlas Steels Co. Ltd. - ATLAS (Mr. L. Wigmore), the Lake Ontario Steel Co. Ltd. - LASCO (Dr. R. Hadden), Stelco Inc. - STELCO (Mr. M. Finn), the Department of Energy, Mines and Resources - CANMET (Dr. J.D. Boyd and Mr. D. Parsons) and the Department of Mechanical Engineering, McMaster University (Dr. I. Yellowley and Dr. H. ElMaraghy).

In this report, Section A contains the results of the materials and machinability characterisation of specific steel grades supplied by individual steel companies, and Section B contains the results of chip formation studies carried out by Dr. S.V. Subramanian.

CONTENTS

SECTION A

		Page
SECTION A1 -	LASCO	A1
	A1.1 INTRODUCTION	A1
	A1.2 MATERIALS CHARACTERISATION	
	A1.2.1 Chemical Analysis	A1
	A1.2.2 Microstructure	A1
	A1.2.3 Inclusion Types	A1
	A1.2.4 QTM. Analysis	A6
	A1.3 MACHINABILITY ASSESSMENT	A6
	A1.3.1 Flank Wear Tests	A11
	A1.3.2 Cutting Forces	A11
	A1.4 DISCUSSION	A16
	A1.5 APPENDIX AA1	A17
SECTION A2 -	ATLAS	A22
	A2.1 INTRODUCTION	A22
	A2.2 MATERIALS CHARACTERISATION	A22
	A2.2.1 Chemical Analysis	A22
	A2.2.2 Microstructure	A22
	A2.2.3 Inclusion Types	A25
	A2.2.4 QTM Analysis	A25
	A2.3 MACHINABILITY ASSESSMENT	A33
	A2.3.1 Flank Wear Tests	A33
	A2.4 DISCUSSION	A33
	A2.5 APPENDIX AA2	A35
SECTION A3 -	STELCO	A37
REFERENCES - SECTION A		
ACKNOWLEDGEMENTS		

CONTENTS

SECTION B

			Page
B1	INTRODUCTION		B1
B2	RESULTS		B1
B3	DISCUSSION		B11
	B3.1	DUCTILE FRACTURE OF CHIPS	B11
	B3.2	DAMAGE AT MODERATE CUTTING VELOCITIES	B14
		B3.2.1 Void Nucleation	B14
		B3.2.2 Void Growth	B18
		B3.2.3 Void Coalescence	B18
	B3.3	NON-UNIFORM VOID DISPERSION	B18
	B3.4	THE EFFECT OF CUTTING VELOCITY	B19
	B3.5	CONCLUSIONS	B21
B4	FUTURE WORK		B23

REFERENCES - SECTION B

ACKNOWLEGEMENTS

SECTION A1 - LASCO

A1.1 INTRODUCTION

Material and machinability characterisation studies were carried out on two AISI 1536 grade steels supplied by LASCO in the form of 2 5/16" D hot-rolled bar stock. Steel A, produced according to LASCO's Al-killed practice, contained 0.028 w/o S and Steel B, which had been ladle injection treated with Ca-Si powder, contained 0.007 w/o S.

A1.2 MATERIALS CHARACTERISATION

A1.2.1 Chemical Analysis

The spectrochemical analyses of the two steels as determined by LASCO and CANMET are given in Table A1.1. The agreement between the two sets of analytical data is good.

A1.2.2 Microstructure (Mr. D. Parsons, CANMET

The microstructure of both steels consisted of fine lamellor pearlite and well distributed ferrite. Representative micrographs of longitudinal sections are presented in Figures A1.1 and A1.2.

A1.2.3 Inclusion Types (Mrs. V. Moore, CANMET)

Mid-radius longitudinal sections from each steel were examined metallographically, Figures A1.3 and A1.4, and the different inclusion types qualitatively identified by microprobe analysis. Steel A contained the typical Al_2O_3 and MnS inclusions normally associated with Al-killed steels while Steel B contained both single phase and duplex globular inclusions, and small single phase MnS inclusions (not observed in Figure A1.4). Quantitative elemental microprobe analyses were carried out on some of the globular duplex inclusions contained in Steel B and the results are presented in Table A1.2. One of the features of the inclusion analysis is the low silicon content.

Table A1.1 - Spectrochemical Analysis - wt. %

Steel Heat No.	Analysis	C	Mn	P	S	Si	Cu	Ni	Cr	Al	Ca
A	CANMET	0.32	1.09	0.010	0.025	0.26	0.18	0.05	0.08	0.018	-
C 8845	LASCO	0.30	1.10	0.010	0.028	0.25	0.18	0.08	0.09	0.016	-
B	CANMET	0.32	1.10	0.010	0.009	0.032	0.13	0.06	0.07	0.019	N.A.
C 9309	LASCO	0.31	1.14	0.011	0.007	0.030	0.15	0.10	0.08	0.024	0.0035

N.A.: Not analyzed.

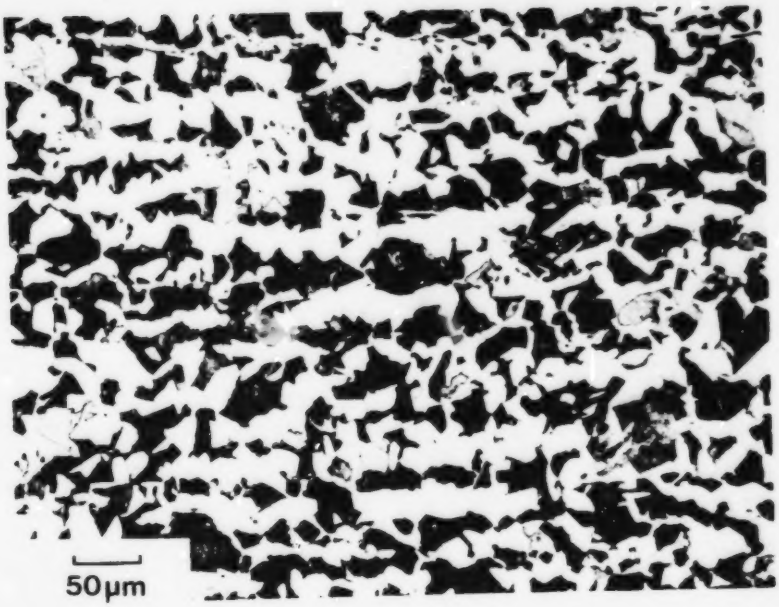

Figure A1.1: Steel A - Microstructure. Longitudinal Section showing fine lamellar pearlite. Etchant 2% nital.

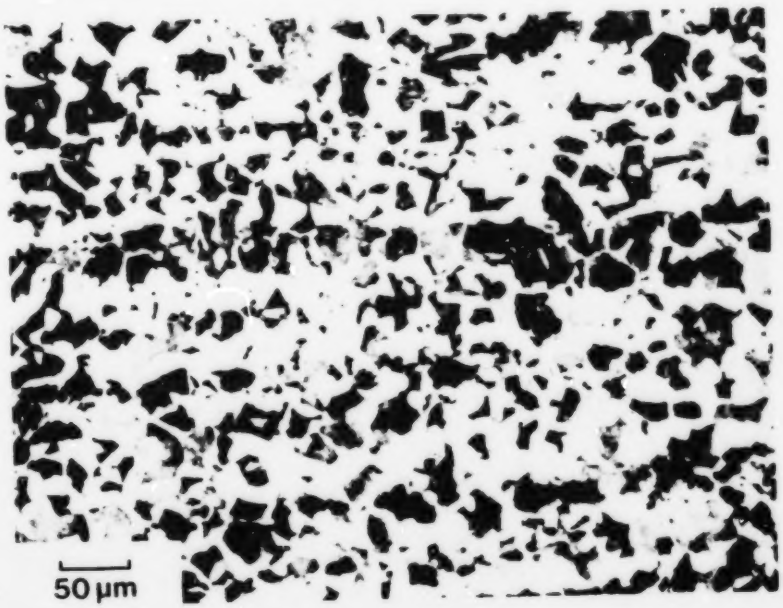

Figure A1.2: Steel B - Microstructure. Longitudinal section showing fine lamellar pearlite. Etchant 2% nital.

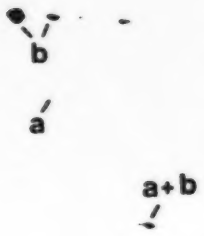

40 µm

Figure A1.3: Steel A: Inclusion types:
a) MnS b) Al_2O_3

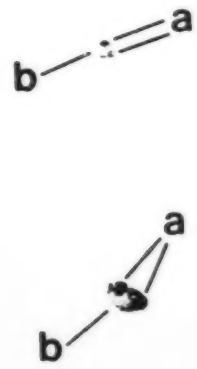

50 µm

Figure A1.4: Steel B: Inclusion types:
(a) Dark area, $CaO.Al_2O_3$
(b) Light area CaS
Small MnS inclusions also observed.

Table A1.2 - Microprobe Elemental Inclusion Analysis - wt %

Inclusion	Al	Ca	Si	S	Mg	Mn	Fe	O†
B-1	25.08	23.18	1.08	0.16	1.27	0.01	0.95	48.28
	26.23	21.57	0.94	0.16	2.47	0.05	1.01	47.58
	25.75	22.65	1.12	0.12	1.62	0.04	0.95	47.77
B-2	32.57	4.30	1.23	0.13	10.40	0.77	1.18	49.42
	27.69	16.72	1.74	0.80	0.07	0.20	2.88	49.89
	33.75	3.13	1.60	0.07	13.49	0.92	1.18	45.86
B-3	18.94	23.61	1.04	12.85	0.0	0.14	3.70	39.72
	4.22	38.35	0.15	30.63	0.0	0.12	3.12	23.42
B-3	1.77	42.20	0.04	34.42	0.0	0.10	2.41	18.07
	27.84	20.34	1.54	0.09	1.63	0.04	2.61	45.91

† Oxygen calculated by difference

The Ca, Al and Mg contents of these inclusions are also given in Table A1.3, together with the corresponding Al/Ca and Al/Ca + Mg molar ratios. According to the $CaO-Al_2O_3$ phase diagram (1) reproduced in Figure A1.5, these molar ratios are consistent with the inclusion types 12 $CaO.7Al_2O_3$, $CaO.2Al_2O_3$ and $CaO.Al_2O_3$. Aluminate inclusions with Al/Ca ratios of < 2 are liquid at steelmaking temperatures and were not observed to be associated with CaS. Aluminate inclusions which were solid at steelmaking temperatures often contained CaS as a major constituent, Figure A1.4, a combination classically associated with good machinability from a tool abrasive wear criterion.

A1.2.4 QTM Analysis (Dr. M. Shehata, CANMET)

The results of the QTM analysis of the oxide and sulphide inclusions in Steels A and B, expressed in terms of their percentage by volume (vol. %), the number of inclusions per mm^2 ($\#mm^2$) and their shape and size are presented in Table A1.4.

The vol. % of oxide inclusions is greater in Steel B than in Steel A, while the vol. % of sulphide inclusions is greater in Steel A than in Steel B. These values are illustrated graphically in Figure A1.6. The respective size distributions, expressed in terms of inclusion length in longitudinal sections, are given in Table AA1.1 and Figures AA1.1 and AA1.2 in Appendix AA1.

A1.3 MACHINABILITY ASSESSMENT (Dr. I. Yellowley and Dr. W. Zaton)

Single point turning machinability tests were carried out on a MAZAK lathe in the Metal Cutting Laboratory at McMaster University.

M2 HSS and Kennametal K-21 carbide tools were used under the following cutting conditions:

Table A1.3 - Inclusion Composition and Type

Inclusion	Ca wt%	Al wt%	Mg wt%	Molar Ratio†		Main Inclusion Types
				Al/Ca	Al/Ca + Mg	
B-1	23.18	25.08	1.27	1.61	1.47	$12CaO \cdot 7Al_2O_3$ and $CaO \cdot Al_2O_3$*
	21.57	26.23	2.47	1.81	1.52	
	22.65	25.75	1.62	1.69	1.51	
B-2	4.30	32.57	10.40	–	2.26	$Ca(Mg)O \cdot Al_2O_3$
	16.72	27.69	0.07	2.46	2.44	
	3.13	33.75	13.49	–	1.98	
B-3	23.61	18.94	0.0	3.70**	–	CaS and $CaO \cdot 2Al_2O_3$
	38.35	4.22	0.0	–	–	CaS
B-4 (Fig. A1.4)	42.20	1.77	0.0	–	–	CaS
	20.34	27.84	1.63	2.03	1.80	$CaO \cdot Al_2O_3$

† Al/Ca ratios. $12CaO \cdot 7Al_2O_3 \equiv 1.2:1$ $CaO \cdot Al_2O_3 \equiv 2:1$ $CaO \cdot 2Al_2O_3 \equiv 4:1$

* Inclusions liquid at steelmaking temperatures.

** Ratio adjusted for CaS content.

Table A1.4 - Quantitative Metallographic Results for LASCO Steels

Steel	Oxide Inclusion > 2 µm					Sulfide Inclusion > 2 µm				
	Vol. %	# mm²	Average Length µm	Average Breadth µm	Average Aspect Ratio	Vol. %	# mm²	Average Length µm	Average Breadth µm	Average Aspect Ratio
A	0.0119	13.5	4.27	2.26	1.90	0.1434	457	3.24	1.31	2.47
B	0.0386	41.9	3.62	2.46	1.65	0.0356	297	1.64	0.92	1.95

Vol. %: Volume % of inclusions ≡ area % of inclusions

mm²: Number of inclusions/mm²

Shape: The average aspect ratio of individual inclusions is not the ratio between the average length and average breadth of all inclusions.

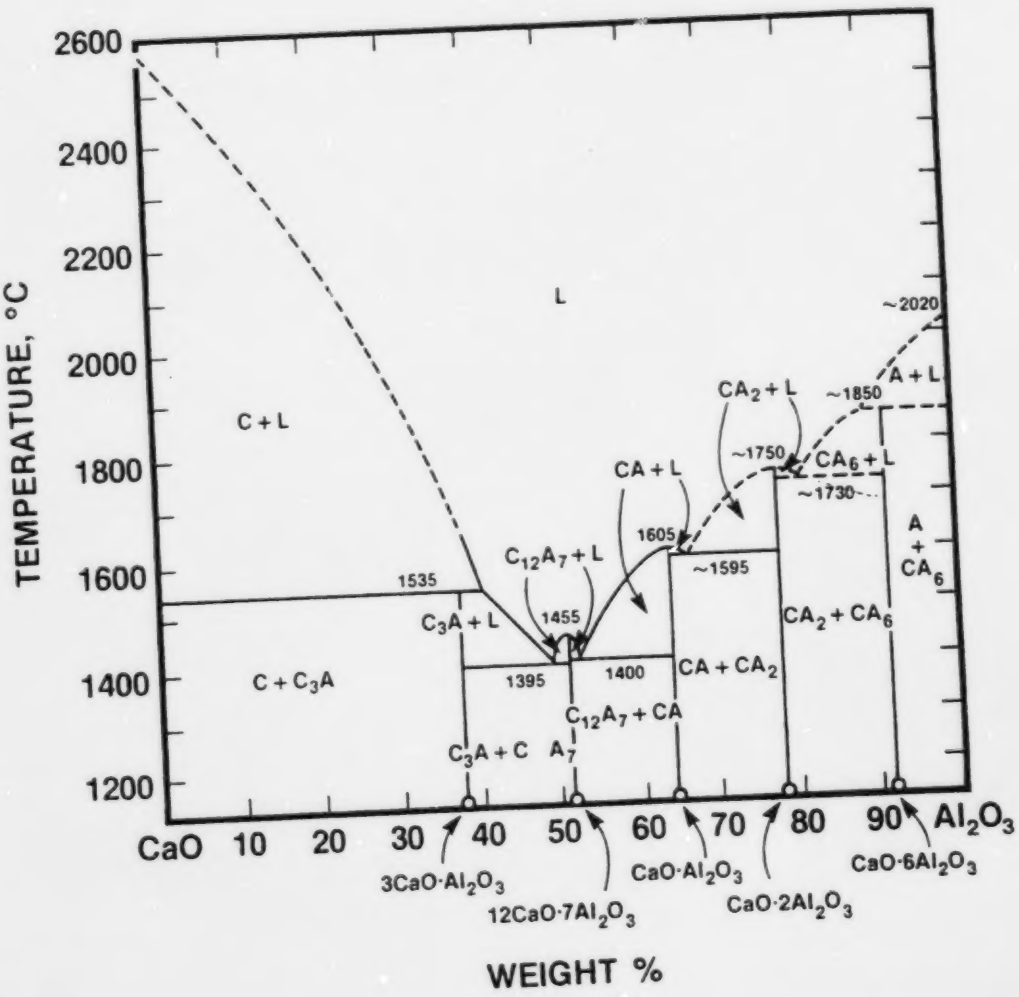

Figure A1.5: The CaO - Al_2O_3 Phase Diagram (1)

	Volume Percent	
	Oxides	Sulphides
Steel A	0.0119	0.1434
Steel B	0.0386	0.0356

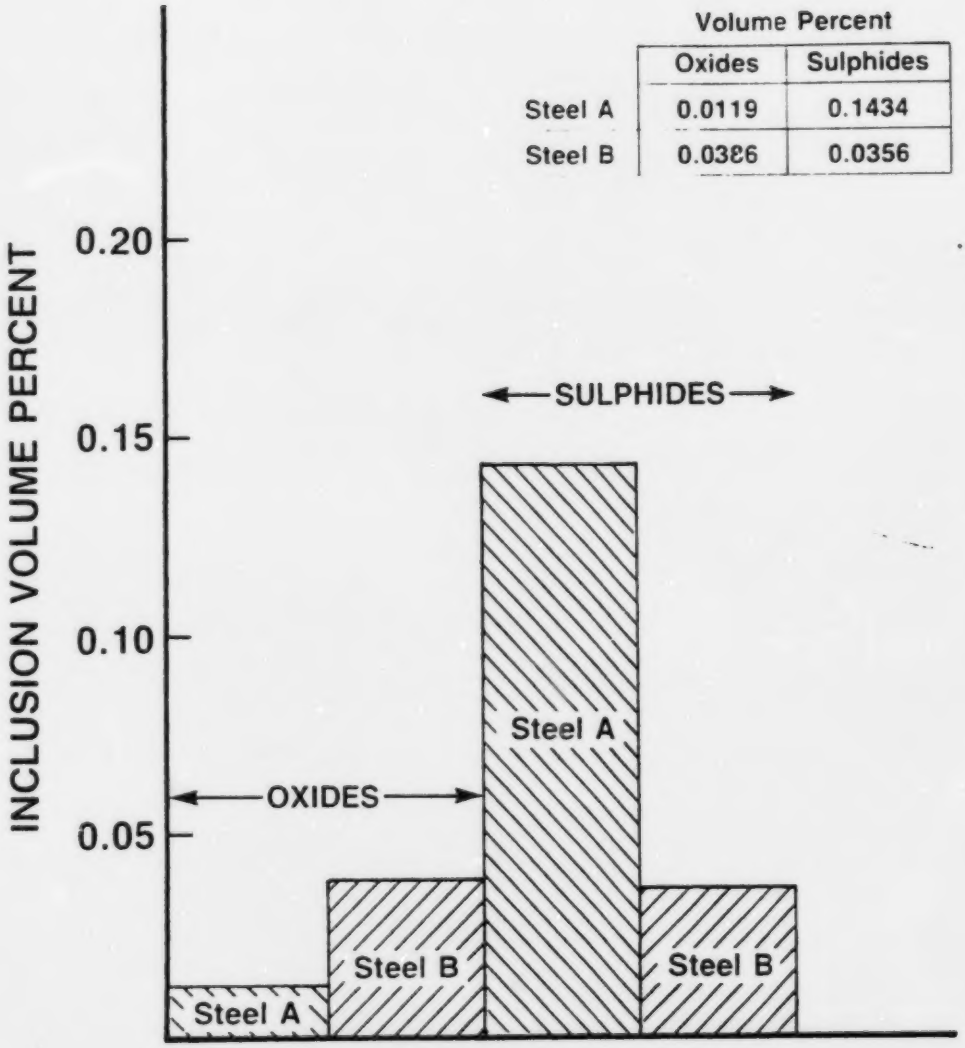

Figure A1.6: Volume Percentage of Oxide and Sulphide Inclusions for LASCO Steels

Tool	K-21 Carbide	M2 HSS
Cutting Speed (v m/min.)	150	50
Feed Rate (f mm/rev.)	0.10	0.10
Depth of Cut (b mm)	2.0	2.0
Rate Angle (α)	10°	15°

No cutting fluid was used.

A1.3.1 Flank Wear Tests

Flank wear test results are presented as a function of cutting time for M2 HSS and K-21 carbide tools in Figures A1.7 and A1.8, respectively.

Flank wear is higher for the M2 HSS tools at a cutting speed of 50 m/min., with Steel A performing marginally better overall than Steel B. At low cutting speeds, however, the formation and relative stability of a built-up edge (BUE) can make the results from tool wear tests inconclusive. Problems arising from BUE formation disappear at higher cutting speeds and the results of tool wear tests for K-21 carbide tools at cutting speeds of 150 m/min. clearly show that Steel B produces less flank wear than Steel A.

A1.3.2 Cutting Forces

In separate tests, the tangential and feed components of the cutting force, F_T and F_N respectively (see Appendix AA1, Figure AA1.3), were measured and the results are presented in Figures A1.9 and A1.10 for M2 HSS and K-21 carbide tools, respectively.

The cutting forces for Steel A using M2 HSS tools are less than those for Steel B but there is no clear distinction between the cutting forces for Steels A and B using K-21 carbide tools.

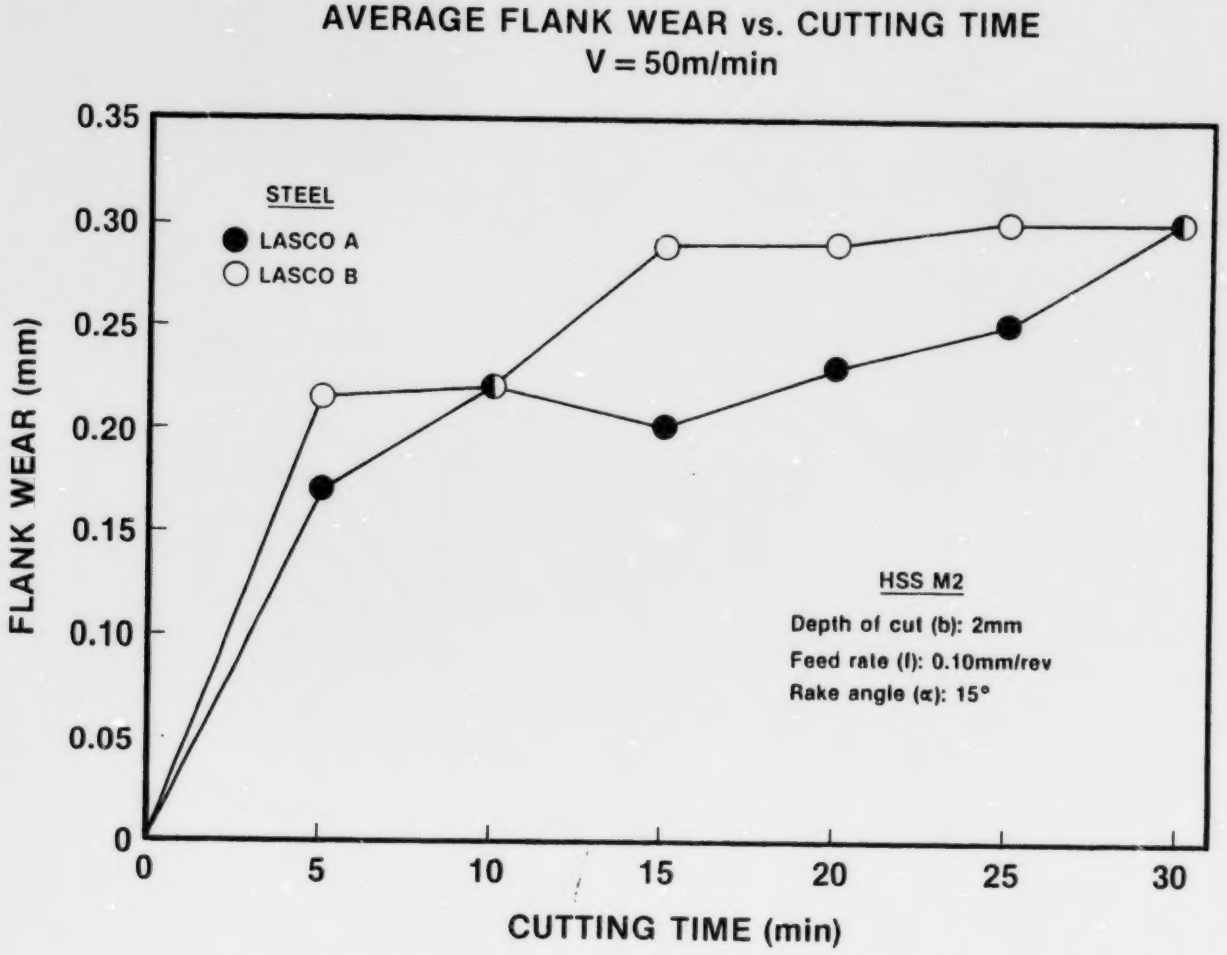

Figure A1.7: Flank Wear vs Cutting Time - M2 HSS

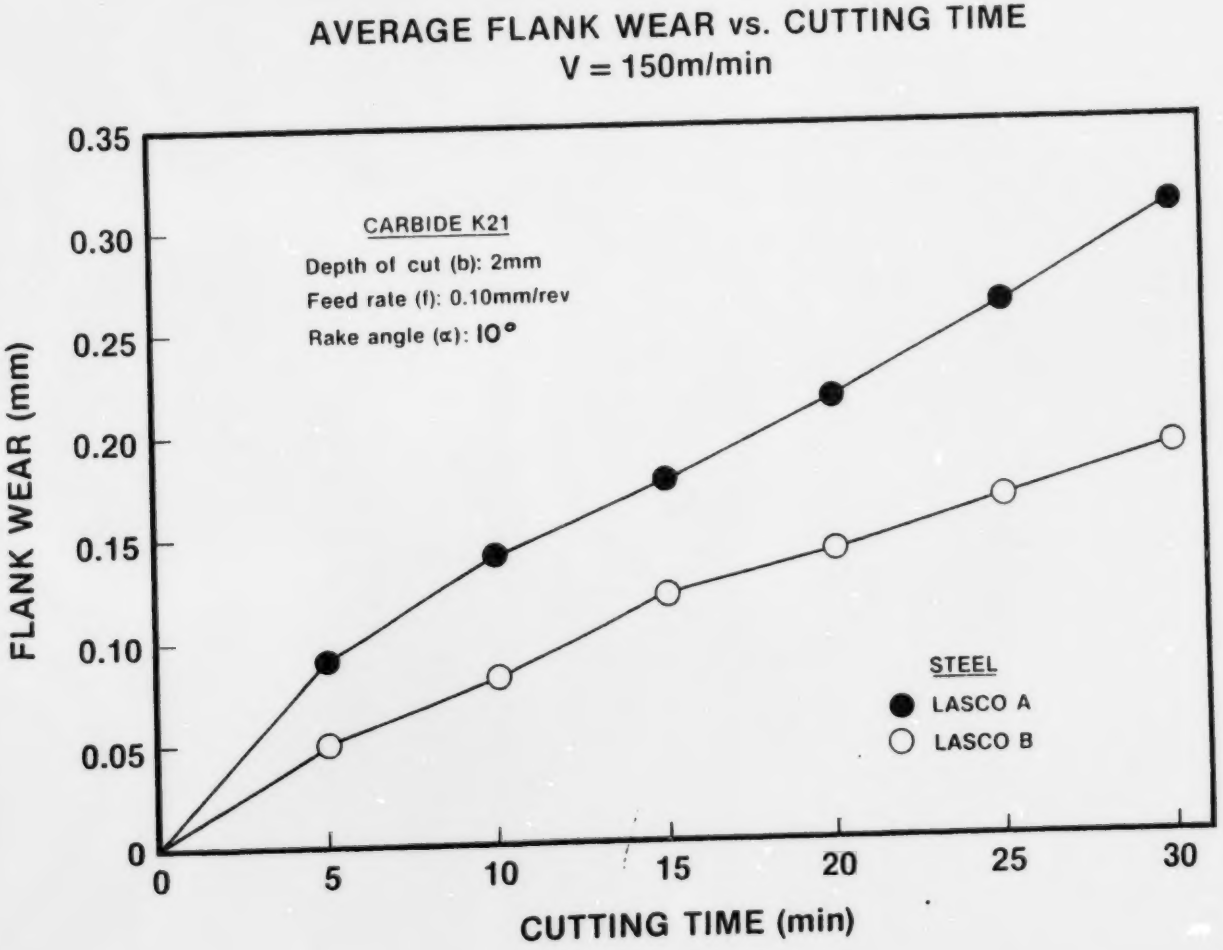

Figure A1.8: Flank Wear vs Cutting Time - K21 Carbide

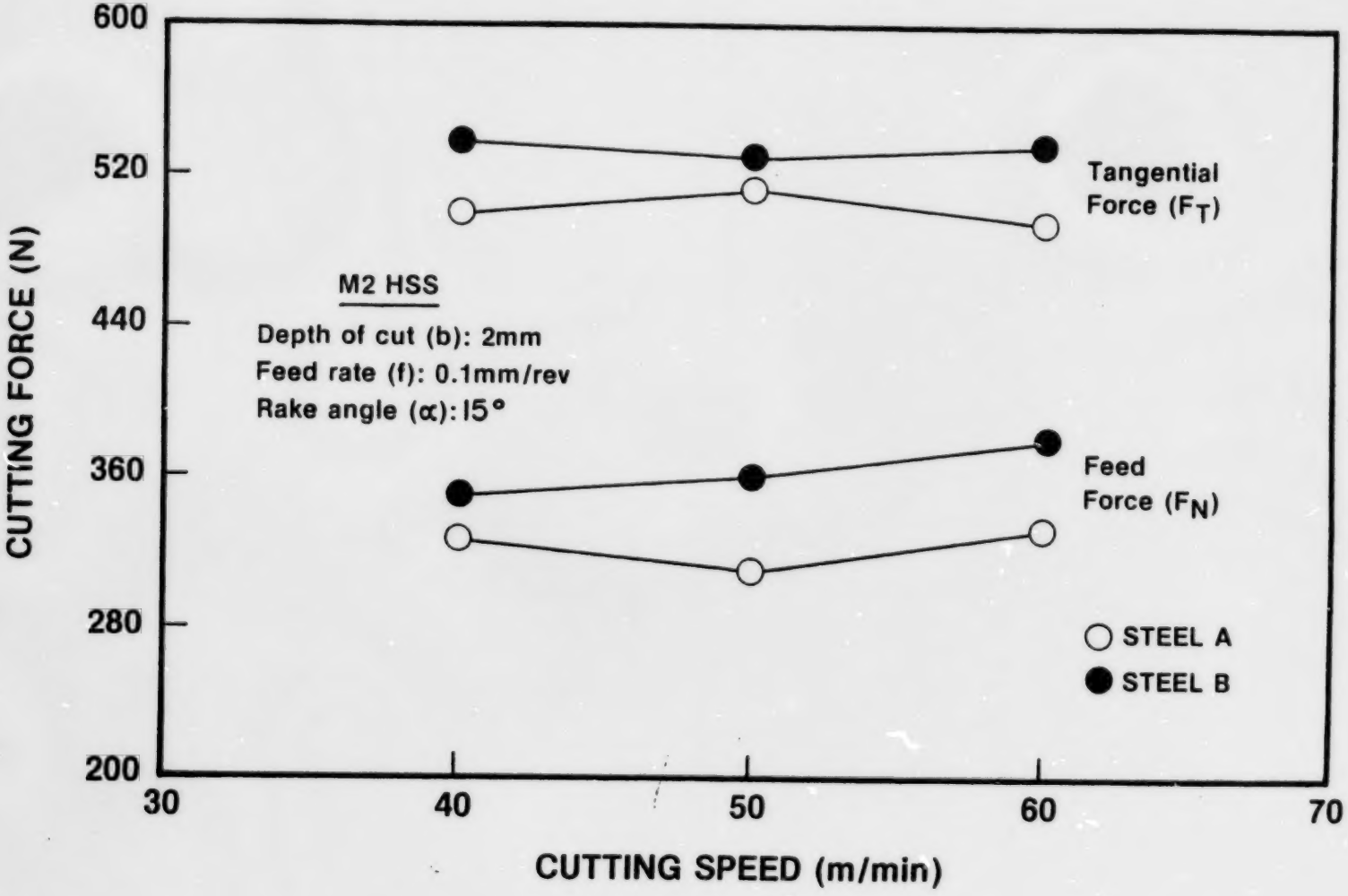

Figure A1.9: Cutting Forces vs Cutting Speed - M2 HSS

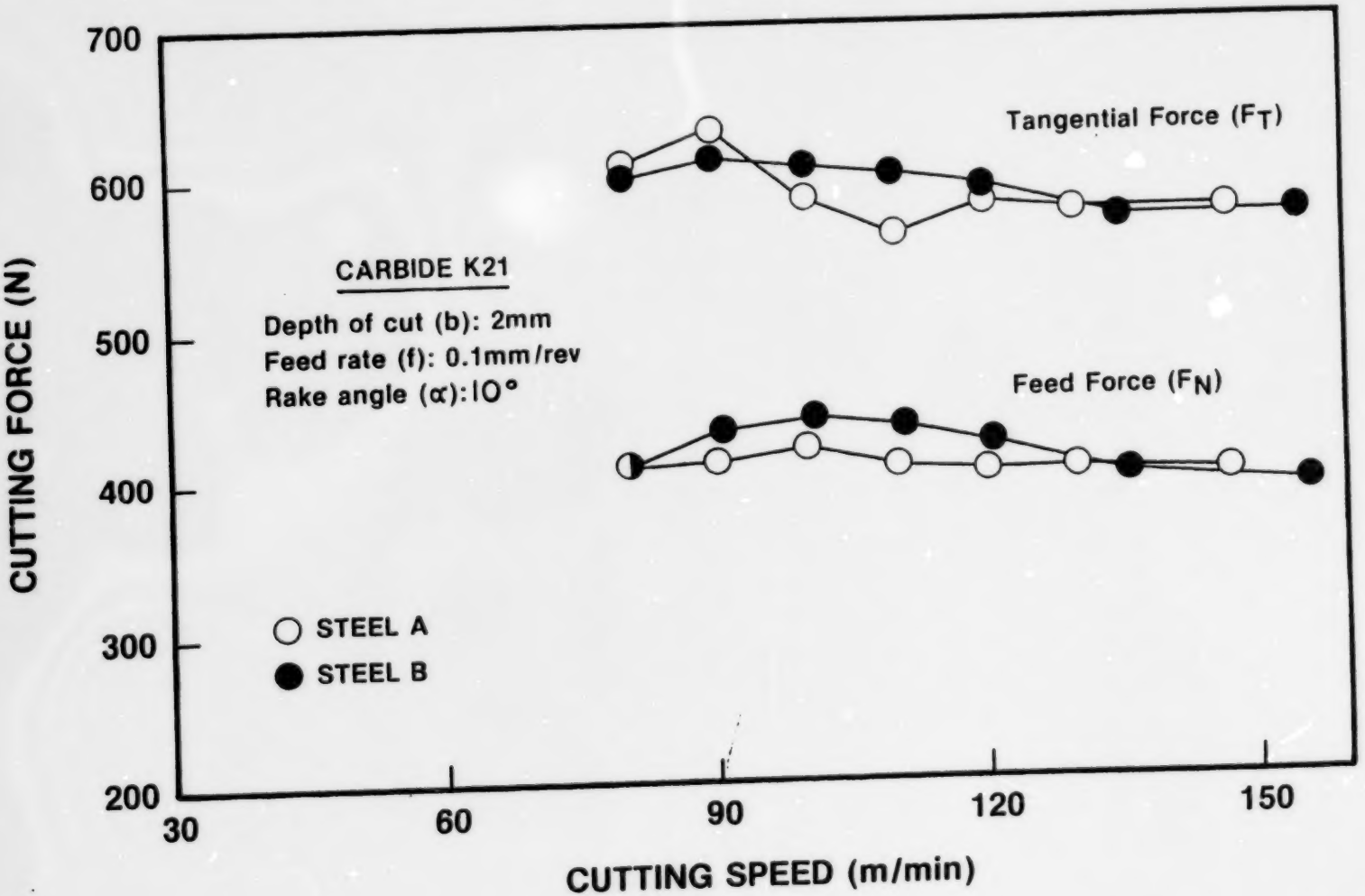

Figure A1.10: Cutting Forces vs Cutting Speed - K21 Carbide

A1.4 DISCUSSION

The steelmaking conditions for Steel B were such that Ca-Si injection yielded calcium aluminate inclusions with a very low silica content. Oxide inclusions which were liquid at steelmaking temperatures, Al/Ca + Mg ratios <2, were not associated with CaS while those which were solid at steelmaking temperatures, Al/Ca + Mg ratios >2, were closely associated with CaS. This combination, despite the fact that Steel B contained more oxide inclusions and less MnS inclusions than Steel A, Figure A1.6, resulted in Steel B giving less tool wear for K-21 carbide tools at a cutting speed of 150 m/min.

The tool wear results for M2 HSS tools, at a cutting speed of 50 m/min, are less conclusive possibly because of built-up edge (BUE) formation.

APPENDIX AAI

Table AA1.1 - Size Distribution of oxides and Sulfides (# cm^2) - LASCO Steels

Size Range μm	Oxides		Sulphides	
	Steel A	Steel B	Steel A	Steel B
0-2	238	1140	18095	26278
2-4	589	1767	17689	2832
4-6	413	840	5488	514
6-8	75	276	2380	63
8-10	12	75	902	38
10-12	-	25	539	25
12-14	-	25	-	13
14-16	-	25	-	13
16-18	-	-	-	-
18-20	-	12	-	-

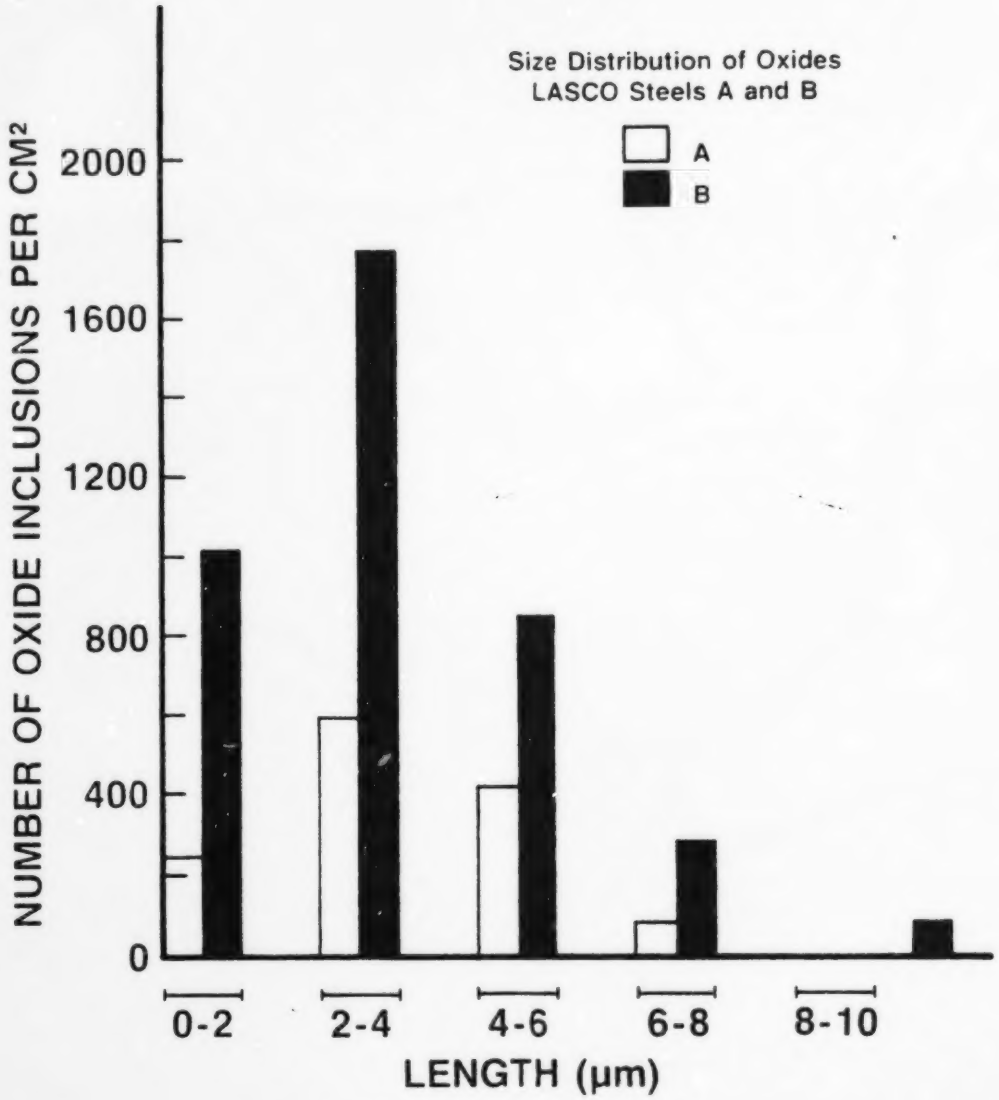

Figure AA1.1: Size Distribution of Oxide Inclusions

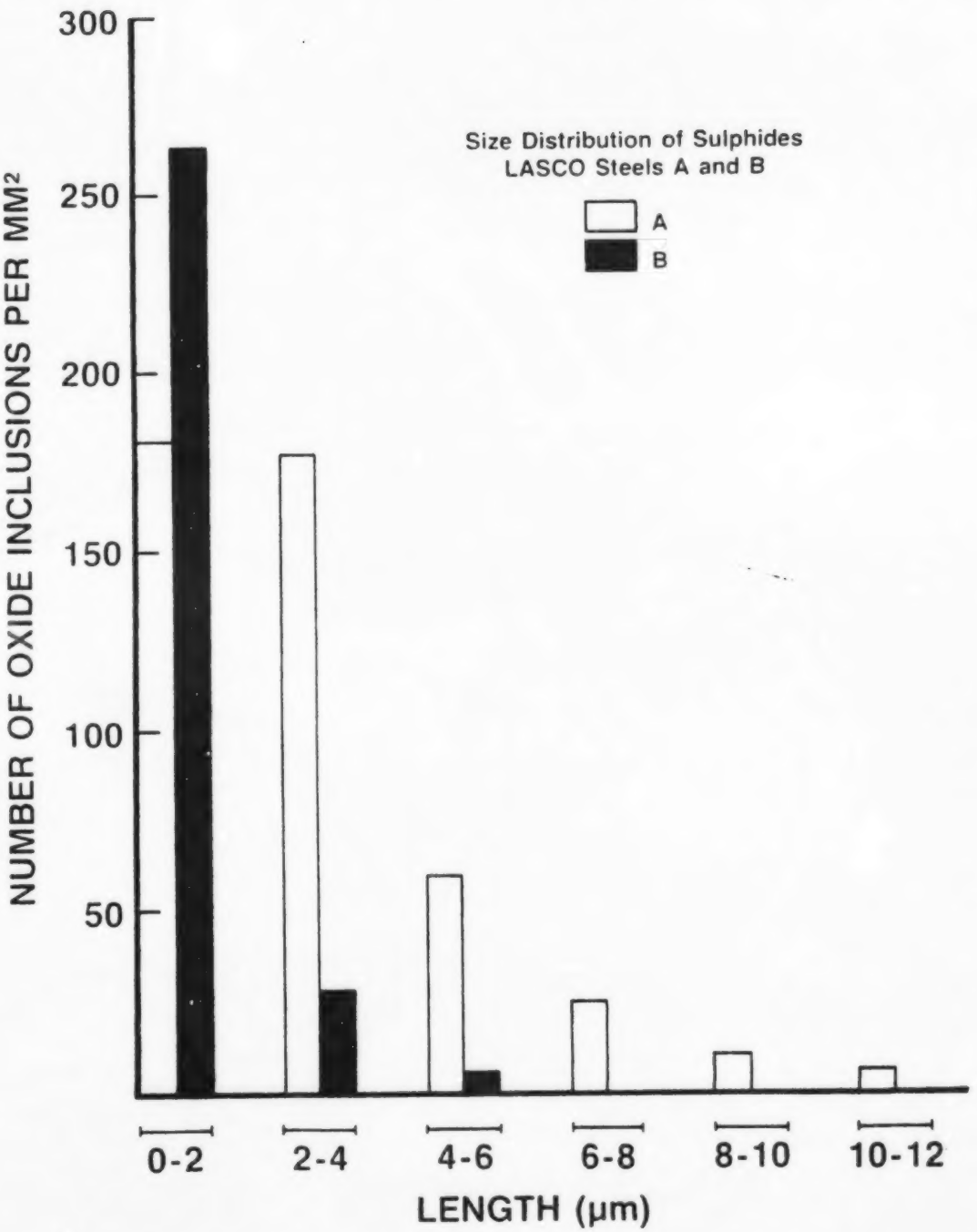

Figure AA1.2 - Size Distribution of Sulphide Inclusions

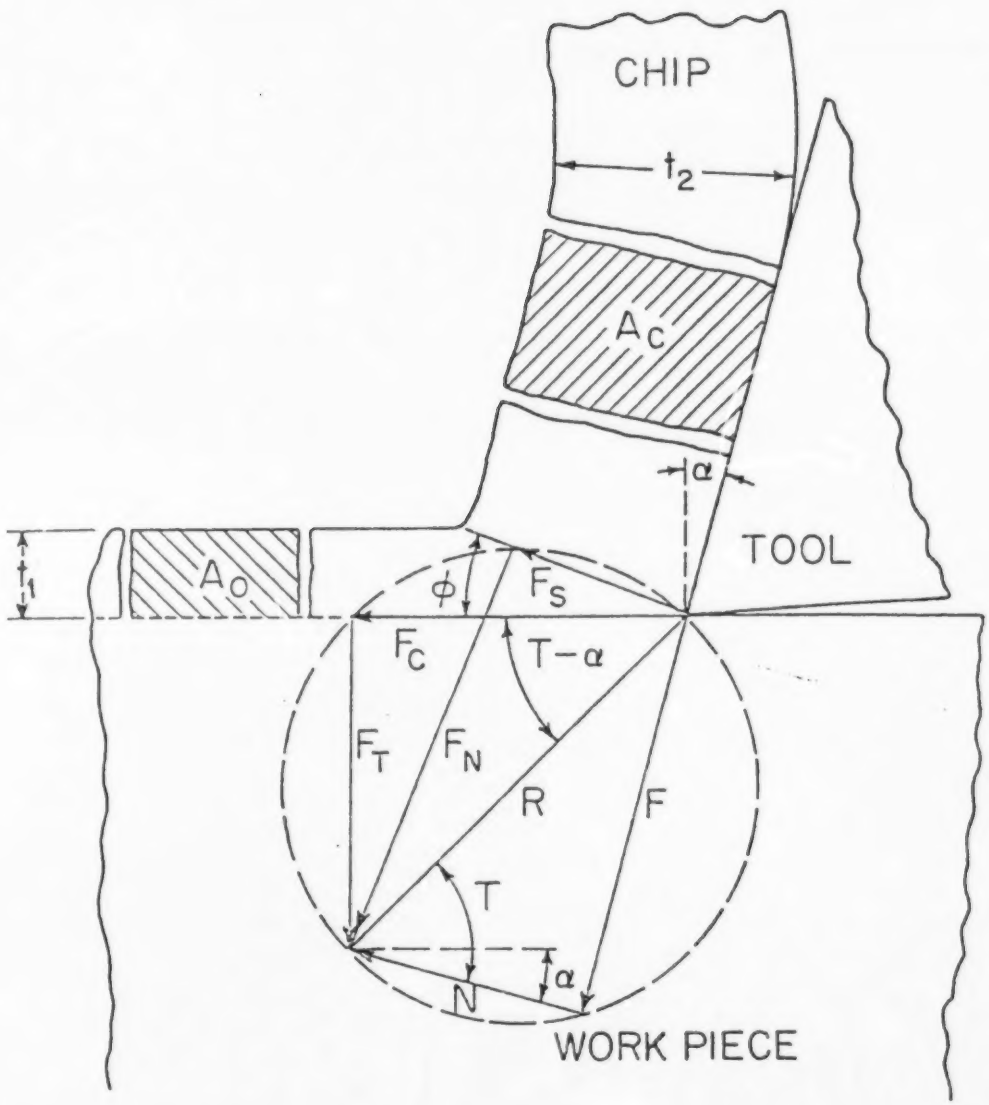

F_T in the text - F_C on this diagram

F_N in the text - F_T on this diagram

Figure AA1.3 - The Composite Force Diagram of Merchant (2)

SECTION A2 - ATLAS

A2.1 INTRODUCTION

Material and machinability characterisation studies were carried out on an AISI 1541 grade steel, designated Steel II, supplied by ATLAS in the form of 1.75" D hot-rolled bar stock, and containing 0.011 w/oS. Preliminary inclusion characterisation of this steel had shown oxide inclusions with compositions in the $CaO.SiO_2$ phase field of the $CaO-Al_2O_3-SiO_2$ phase diagram, close to the $CaO.SiO_2/CaO.Al_2O_3.2SiO_2/2CaO.Al_2O_3.SiO_2$ ternary eutectic composition. On the basis of this oxide inclusion analysis, the machinability of Steel II with respect to tool wear, was expected to be good.

The results of the characterisation studies for Steel II are compared with those for a Si-Al killed AISI 1541 steel containing ~ 0.075 w/o S, designated Steel I, which was also supplied by ATLAS and designed to contain Al_2O_3 and MnS inclusions. The results for Steel I are taken from the Phase III Final Report (3) of this project.

A2.2 MATERIALS CHARACTERISATION

A2.2.1 Chemical Analysis

The spectrochemical analysis of the two steels provided by ATLAS and CANMET are given in Table A2.1. In comparing the analysis for Steels I and II, the differences in aluminum content, 0.04 w/o vs. ~ 0.0035 w/o respectively, and sulphur content, 0.075 w/o vs. 0.011 w/o respectively, are to be noted.

A2.2.2 Microstructure

The microstructure of both steels consisted of five lamellar pearlite and well distributed ferrite. Representative micrographs of transverse sections are presented in Figures A2.1 and A2.2.

Table A2.1 – Spectrochemical Analysis – wt %

Steel	Analysis	C	Mn	P	Si	Ni	Al	Nb	Cr	S	Cu	O	N
1541	CANMET	0.42	1.19	0.015	0.215	0.155	0.040	<0.005	0.145	0.080	-	N.A.	N.A.
I	ATLAS	0.39	1.11	0.016	0.290	0.150	0.040	N.A.	0.150	0.069	-	N.A.	N.A.
1541	CANMET	0.42	1.59	0.017	0.240	0.17	0.002	0.034	0.036	0.011	N.A.	N.A.	N.A.
II	ATLAS	0.40	1.35	-	-	-	0.005	0.040	-	-	0.0043	0.0095	0.006

N.A.: Not analysed

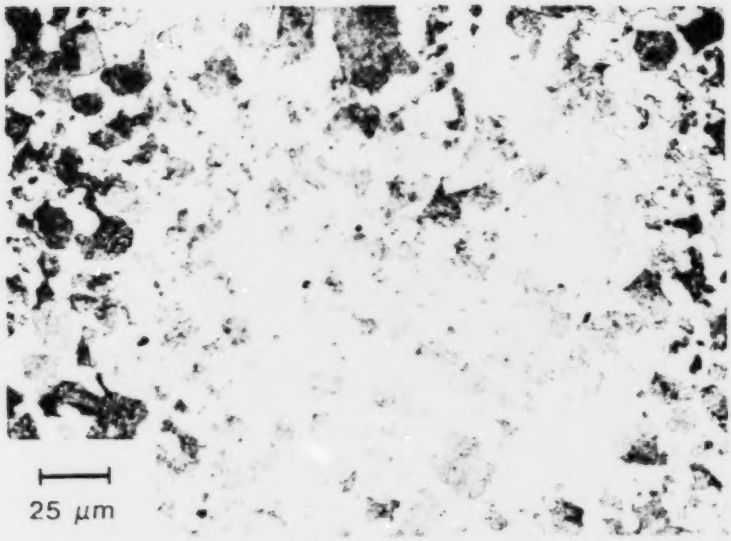

Figure A2.1: Steel I: Microstructure. Transverse Section showing fine lamellar pearlite with good ferrite distribution. Etchant 2% nital.

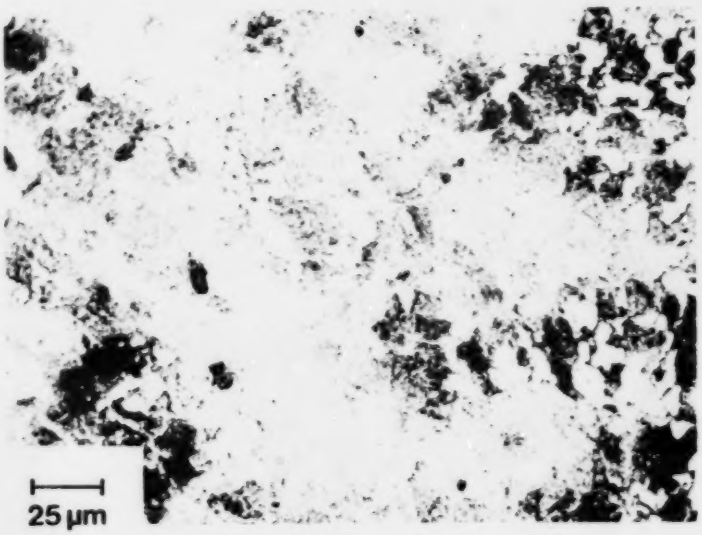

Figure A2.2: Steel II: Microstructure. Transverse Section showing fine lamellar pearlite with good ferrite distribution Etchant 2% nital.

A2.2.3 Inclusion Types (Mrs. V. Moore, CANMET)

Mid-radius longitudinal sections from each steel were examined metallographically and the different inclusion types qualitatively identified by microprobe analysis. Quantitative elemental microprobe analyses were carried out on representative inclusions.

Steel I, Figure A2.3, contained elongated MnS inclusions in which Al_2O_3 inclusions were embedded. Steel II contained both elongated single phase oxide and MnS inclusions, Figure A2.4, and elongated duplex MnS inclusions with oxide tips, Figure A2.5.The microprobe elemental inclusion analysis is presented in Table A2.2.

The elemental Ca, Al and Si contents of the oxide inclusions in Steel B expressed in terms of the weight percent contents of their respective oxides - CaO, Al_2O_3 and SiO_2 - and normalised to 100%, are given in Table A2.3. The inclusion type, also given in this Table A2.3, was determined by plotting the base percentage oxide contents on a ternary CaO-Al_2O_3-SiO_2 phase diagram, Figure A2.6, which also contains the base composition of the oxide inclusions in the preliminary characterisation.

The high silicon content of the CaO-Al_2O_3-SiO_2 base composition, together with the high MnO and FeO contents, indicate that Steel II has either been weakly deoxidised or substantially reoxidised.

A2.2.4 QTM Analysis (Dr. M. Shehata, CANMET)

The results of the QTM analysis of the oxide and sulphide inclusions in Steels I and II, expressed in terms of their percentage by volume (vol. %), the number of inclusions per mm^2(# mm^2) and their shape and size are presented in Table A2.4.

The vol. % of oxides is greater in Steel II than in Steel I while the large difference in the vol. % of sulphide inclusions reflects the higher sulphur content of Steel I, 0.075 w/o. These values are illustrated graphically in Figure A2.7. The respective size distributions

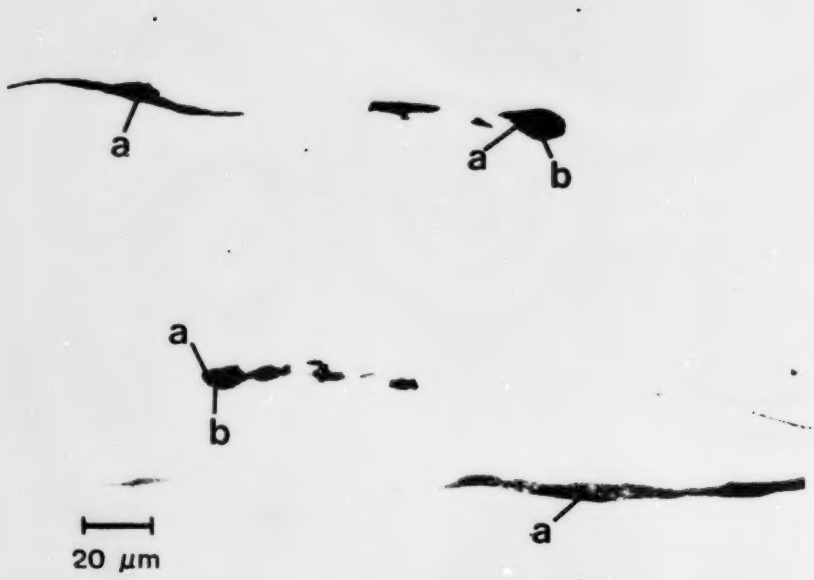

Figure A2.3: Steel I: Inclusion types
(a) MnS (b) Al_2O_3

25μm

Figure A2.4: Steel II: Inclusion types
(a) $CaO.SiO_2$ (b) MnS

25μm

Figure A2.5: Steel II: Inclusion types.
(a) $CaO.SiO_2$ (b) MnS

Table A2.2 – Microprobe Elemental Inclusion Analysis – wt %

Inclusion	Al	Si	Mg	S	Ca	Mn	Fe	Ti	O*
Fig. A2.4 (a)	2.46	16.64	0.0	0.20	15.85	13.45	12.92	1.55	36.93
	3.96	15.40	0.02	0.08	12.19	10.56	15.16	2.60	40.02
	3.02	16.91	0.0	0.72	15.87	18.78	4.04	0.83	39.83
	3.23	15.19	0.0	0.21	12.84	11.45	8.45	1.68	46.95
Fig. A2.5 (a)	2.50	15.40	0.0	0.98	10.94	19.00	13.6	1.15	4.96
	4.56	14.41	0.0	0.96	9.08	14.26	35.67	2.25	36.43
Fig. A2.5(b)	0.02	0.02	0.0	33.15	0.12	59.01	2.72	0.01	18.81

* Oxygen calculated by difference

Table A2.3 – Oxide Inclusion Composition – wt. %

Inclusion	Ca w/o	Al w/o	Si w/o	$(CaO + SiO_2 + Al_2O_3) \equiv 100$			Primary Type
				CaO	SiO_2	Al_2O_3	
	15.55	2.46	16.64	35.5	57.1	7.4	$CaO{\cdot}SiO_2$
Fig. A2.4	12.19	3.96	15.40	29.6	57.4	13.0	$CaO{\cdot}SiO_2$
(a)	15.87	3.02	16.91	34.6	56.5	8.9	$CaO{\cdot}SiO_2$
	12.84	3.23	15.19	31.7	57.5	10.8	$CaO{\cdot}SiO_2$ +
Fig. A2.5	10.94	2.50	15.40	28.9	62.2	8.9	$CaO{\cdot}SiO_2$
(a)	9.08	4.56	14.41	24.3	59.2	16.5	$CaO{\cdot}Al_2O_3{\cdot}2SiO_2$

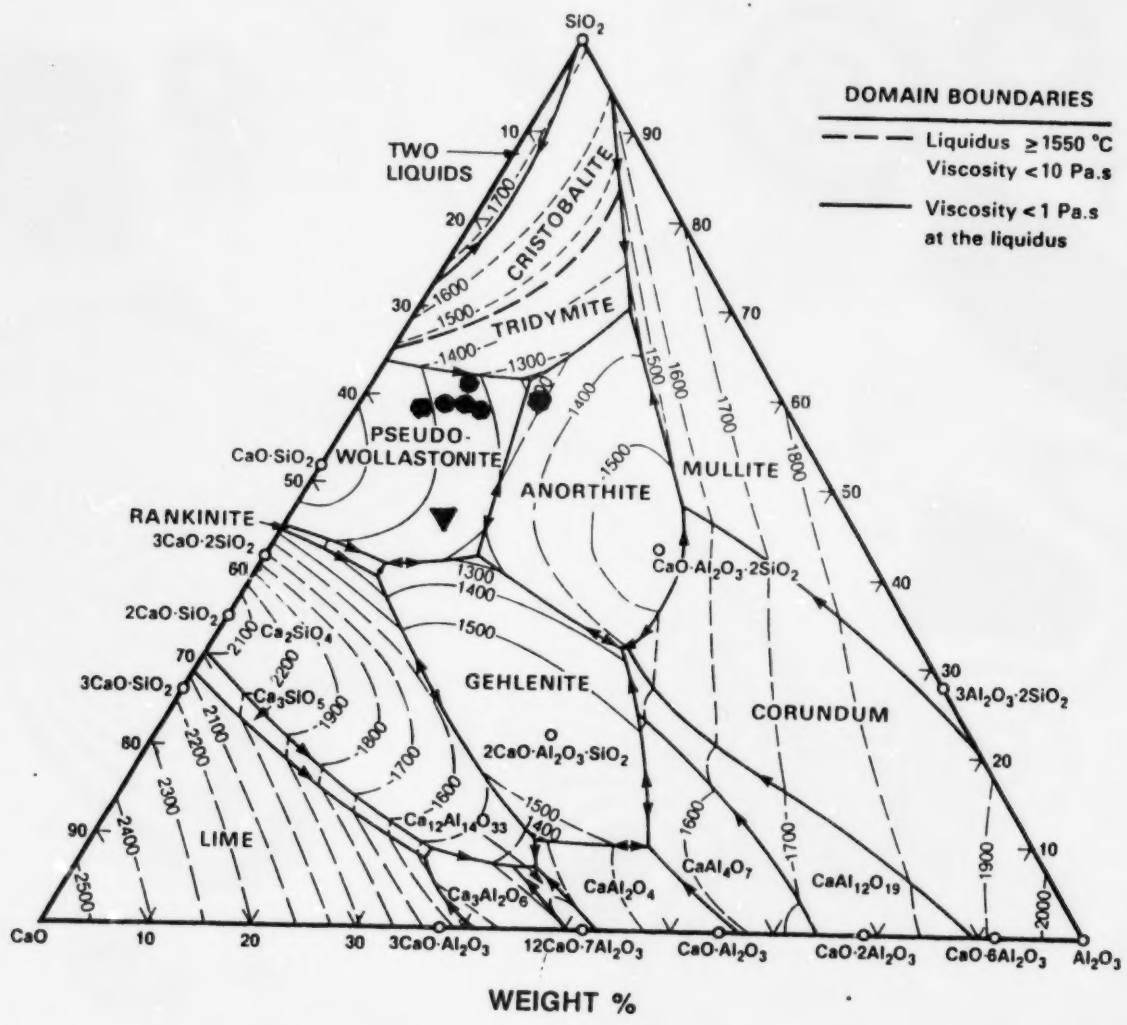

Figure A2.6: The $CaO - Al_2O_3 - SiO_2$ Phase Diagram (4)

● - Base composition of oxide inclusions given in Table A2.3

▼ - Preliminary characterization

Table A2.4 - Quantitative Metallographic Results for ATLAS Steels

Steel	Oxide Inclusion					Sulfide Inclusion				
	Vol. %	#/mm²	Average Length µm	Average Breadth µm	Average Aspect Ratio	Vol. %	# mm²	Average Length µm	Average Breadth µm	Average Aspect Ratio
I	0.0228	4.8	5.86	4.58	1.37	0.367	168	8.76	3.18	2.42
II	0.0276	19.4	6.05	2.32	2.84	0.082	192	3.72	1.25	2.83

	Volume Percent	
	Oxides	Sulphides
Steel I	0.0228	0.367
Steel II	0.0276	0.082

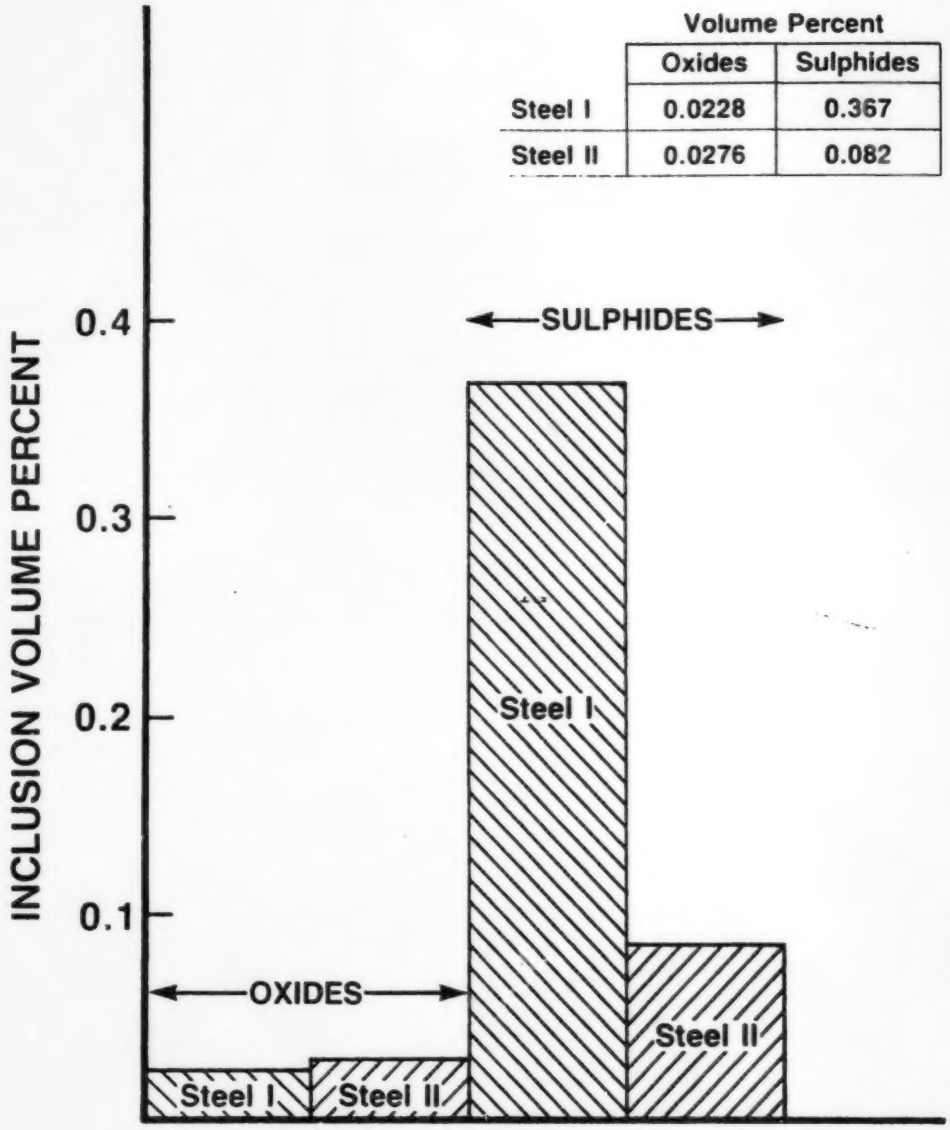

Figure A2.7: Volume Percentage of Oxide and Sulphide Inclusions for ATLAS Steels

(number of inclusions for cm^2 - # cm^2), expressed in terms of inclusion length in longitudinal sections, are given in Table AA2.1 in the Appendix AA2.

A2.3 MACHINABILITY ASSESSMENT (DR. I. YELLOWLEY AND DR. W. ZATON)

Single point turning machinability tests were carried out on Steels I and II using a MAZAK lathe in the Metal Cutting Laboratory at McMaster University.

Kennametal K-21 carbide tools were used under the following cutting conditions:

Cutting Speed (v m/min.)	150
Feed Rate (f mm/rev.)	0.176
Depth of Cut (6 mm)	2.0
Rate angle (α)	10°

No cutting fluid was used.

A2.3.1 Flank Wear Tests

Flank wear test results are presented as a function of cutting time in Figure A2.8 where it can be seen that the flank wear is substantially higher for Steel II.

A2.4 DISCUSSION

In Steel II the presence of CaO-SiO_2 based inclusions containing substantial quantities of iron and manganese oxides is indicative of re-oxidation during the latter stages of steelmaking. These oxide inclusions are seldom associated with MnS inclusions because of the relatively low sulphur content (0.007 wt %), see Figures A2.4 and A2.5.

In Steel I, which has a relatively high sulphur content (0.07 wt. %) the more abrasive Al_2O_3 inclusions are closely associated with massive MnS inclusions, Figre A2.3. This combination in Steel I has resulted in Steel I giving less tool wear than Steel II when machining with K21 carbide tools at a cutting speed of 150 m/min, see Figure A2.8.

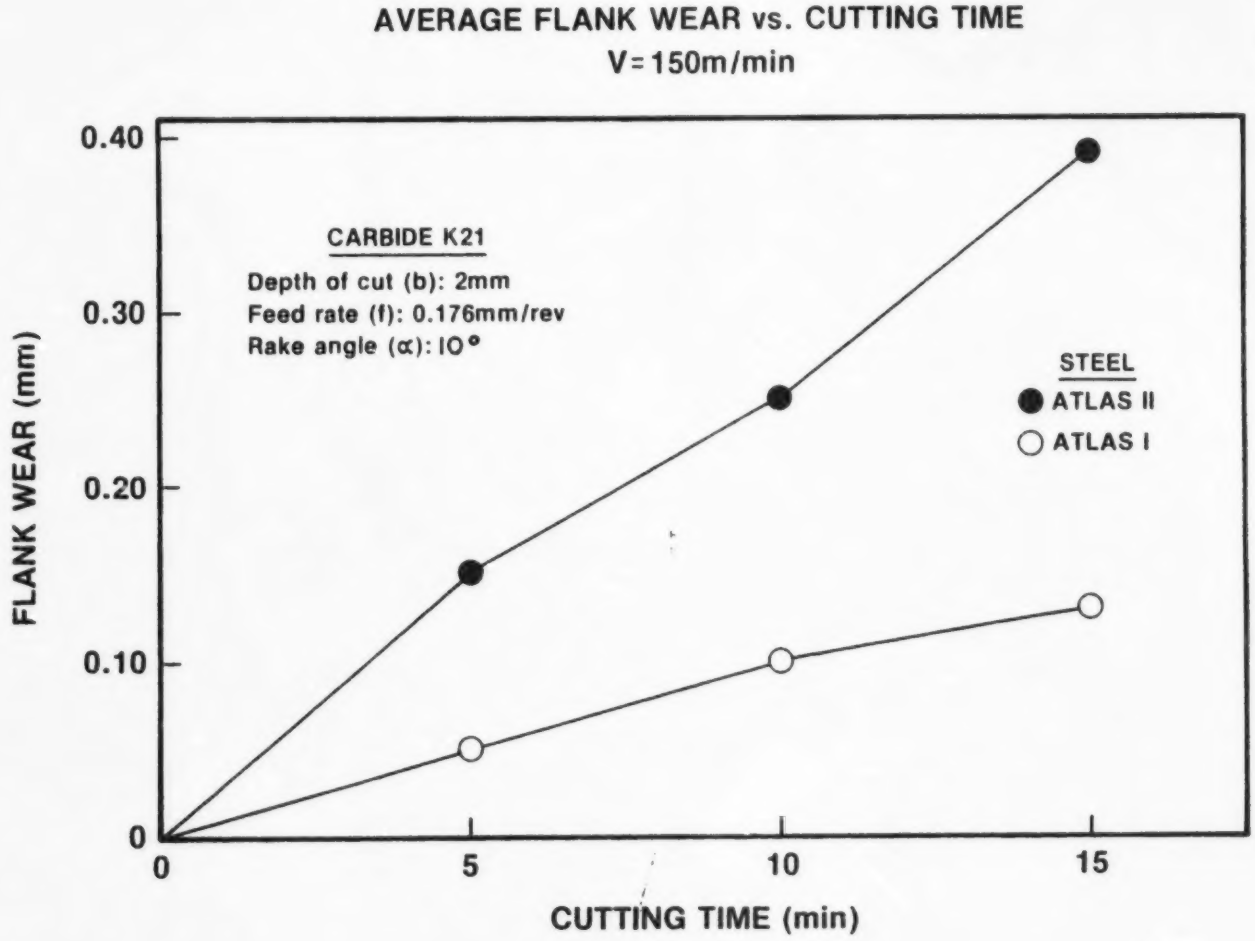

Figure A2.8: Flank Wear vs Cutting Time - K21 Carbide

APPENDIX AA2

Table AA2.1 - Size Distribution of Oxides and Sulphides (# cm^2) - ATLAS Steels.

Size Range (μm)	Steel I		Size Range (μm)	Steel II	
	Oxides	Sulphides		Oxides	Sulphides
0-5	276	9623	0-2	313	8471
5-10	138	3139	2-4	426	6165
10-15	40	1395	4-6	551	1904
15-20	24	871	6-8	213	1102
20-25	2	442	8-10	139	526
25-30	0	336	10-12	175	226
30-35	0	294	12-14	38	188
35-40	0	204	14-16	26	113
40-45	0	95	16-18	26	113
45-50	0	93	18-20	0	38
50-55	0	76	20-22	0	63
55-60	0	56	22-24	0	38
60-65	0	49	24-26	0	50
65-70	0	28	26-28	13	38
70-75	0	25	28-30	13	13
75-80	0	16	30-32	0	25
80-85	0	7	32-34	0	0
85-90	0	2	34-36	13	25
90-95	0	0	36-38	0	0
95-100	0	9	38-40	0	13
100-105	0	5	40-42	0	0
105-110	0	7	42-44	0	0
110-115	0	7	44-46	0	13
115-120	0	5	46-48	0	0
120-125	0	7	48-50	0	0
>125	0	9	>50	0	38

SECTION A3 - STELCO

A preliminary investigation was carried out on an AISI 1070 Grade steel, which had been subjected to various heat treatments, in an attempt to relate cutting forces to the results of form turning tests (ASTM E618-81). The various heat treatments resulted in fine pearlite, coarse pearlite and partially spheroidised microstructures.

The 7/8"D AISI 1070 bars supplied, however, proved to be of too small a diameter for reliable dynamometer tests to be made and cutting force measurements in both longitudinal and transverse directions to the bar axis proved to be insensitive to the microstructural variations, and hence to the mechanical properties.

Tensile test load/elongation curves were found to be much more sensitive to the microstructural variations and could therefore be related to the results of the form turning tests. Thus, a steel with a partially spheroidised microstructure, having a lower yield strength than a corresponding steel with a fine pearlite microstucture, yielded three times as many machined parts. A steel with a coarse pearlite microstructure yielded intermediate results.

The theoretical basis for the influence of microstructure on machinability is discussed in Section B of this report.

SECTION A - REFERENCES

1. G.A. Rankin and F.E. Wright: "The Ternary System $CaO-Al_2O_3.SiO_2$", Am. J. Sci., vol. 39, 1915, pp. 1-79.

2. M.E. Merchant: J. App. Phys., Vol. 16, No. 5, 1945, pp. 267-275.

3. S.V. Subramanian, V. Meng and D.A.R. Kay, "Development of Non-Leaded Free Machining Steels - Phase III". Final Report, April 1, 1983 - March 31, 1984. D.S.S. File No. 13SV-23440-3-9134.

4. A. Muan, E.F. Osborn: 'Phase Equilibria Among Oxides in Steelmaking", Addison-Wesley Publishing Co. June., 1965.

ACKNOWLEDGEMENTS

The authors should like to acknowledge the finanacial support of the Department of Energy Mines and Resoures (CANMET). Materials characterization was carried out by CANMET and the work of Dr. J. D. Boyd, Mr. D.A. Parsons, Dr. M. Shehata and Mrs. Vera Moore is gratefully acknowledged. Machinability tests were carried out in the Department of Mechanical Engineering, McMaster University, and the work of Dr. H. ElMaraghy, Dr. I. Yellowley and Dr. W. Zaton is gratefully acknowledged. The authors would also like to acknowledge the cooperation of Dr. R. Hadden of Lake Ontario Steel Co. Ltd., Mr. Larry Wigmore of Atlas Steels Co. Ltd. and Mr. M. Finn of Stelco Inc., in supplying the steels which are the basis of the report.

SECTION B

STUDIES ON CHIP FORMATION

B1 INTRODUCTION

In order to understand the influence of the microstructure on the micromechanisms of the fracture processes that are involved during chip formation in different grades of steel, a number of quick-stop samples obtained from low speed (< 200 m/min.) orthogonal cutting processes were examined using metallographic and electron-optical (SEM/TEM) techniques. At higher cutting speeds (> 200 m/min.), quick-stop samples could not be obtained and only the chips, generated during machining, were examined under the SEM.

Quick-stop samples obtained from AISI grades 1018, 1040 and 4340 at cutting speeds of 73 and 110 m/min. were examined. Chips from two CK45 grades of two different sulfur levels, 0.035 and 0.056 wt. %, and produced at cutting speeds of 200 and 2000 m/min. respectively, were obtained from IFW, University of Hanover, and also examined.

B2 RESULTS

Figure B1(a) shows a quick-stop sample of a continuous chip resulting from the orthogonal cutting of a typical low carbon resulfurised mild steel. The microstructure essentially consists of a ferritic matrix with a small volume fraction (< 5%) of pearlite. The elongated MnS inclusions with aspect ratios of over 10 occur in the ferritic phase. Figure B1(b) shows a montage of SEM pictures showing the primary and secondary shear zones. An important feature to note is the presence of voids associated with the fragmented cementite particles in those pearlite lamellae that are oriented parallel to the tensile direction in the primary shear zone. By comparison, the elongated MnS inclusions occurring adjacent to the pearlite with an identical orientation to the pearlite in the primary shear zone do not show any cracking. Figure B2, and void nucleation, if any in this case, is confined to the tips of the elongated inclusions. However, those elongated MnS inclusions that are oriented

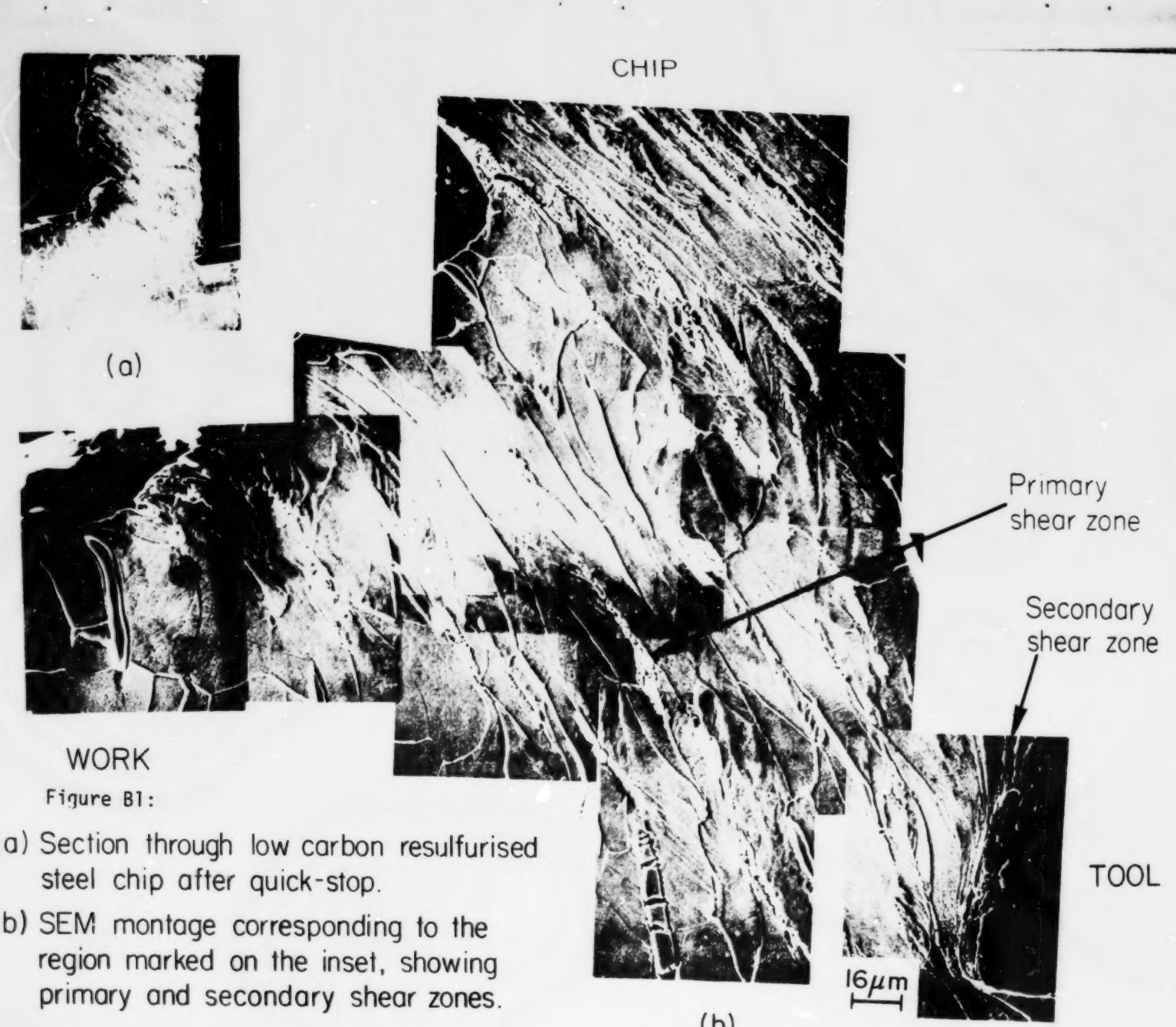

Figure B1:

(a) Section through low carbon resulfurised steel chip after quick-stop.

(b) SEM montage corresponding to the region marked on the inset, showing primary and secondary shear zones.

Figure B2:

Fragmentation of carbides in the primary shear zone.

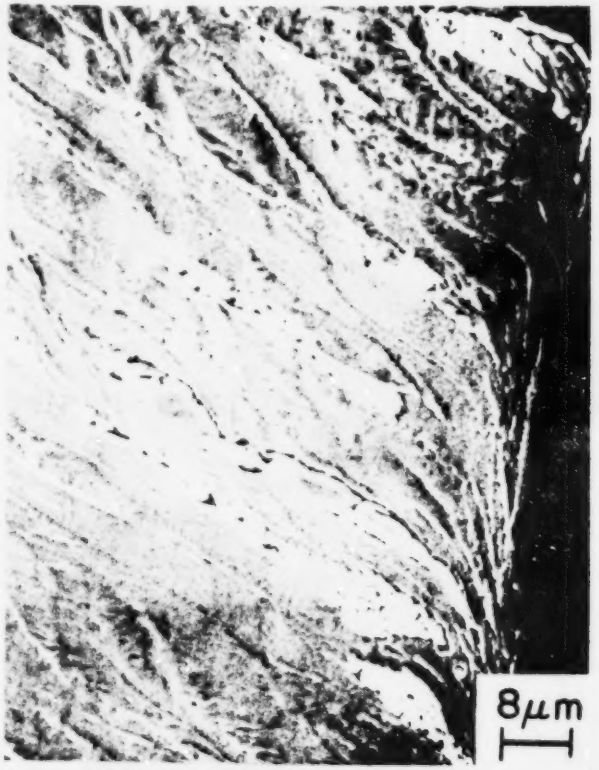

Figure B3:

Decohesion at the MnS/matrix interface in the secondary shear zone.

transverse to the tensile axis have undergone fragmentation. There is also evidence of decohesion at the MnS/matrix interface in the secondary shear zone, Figure B3.

If the pearlite lamellae are oriented transverse to the tensile stress direction and the pearlite colony is small, the pearlite lamellae are sheared and displaced. Figure B4 is an SEM picture showing typical shearing of the pearlite lamellae encountered in the primary shear zone of an AISI 1018 steel grade machined at a cutting speed of 73 m/min. Figures B5 and B6 show TEM pictures of plastic replicas taken of the lamellar pearlite oriented parallel and transverse to the tensile stress axis in the primary shear zone, respectively, obtained from a quick stop sample of an AISI 1018 steel grade machined at a cutting speed of 110 m/min. Figure B5 shows the complete fragmentation of the cementite, when fibre loading of the cementite has occurred; Figure B6 shows the shearing of the pearlite.

As the volume fraction of pearlite is increased or as the pearlite colony size becomes bigger, as in an AISI 1040 steel grade, there is evidence of local deformation within a colony in the primary shear zone. This is reflected by the local deformation of the lamellae within a colony. However there is no evidence of void formation. On the other hand, the inclusions in this case are associated with significant void growth and linkage. Figure B7 shows a montage of SEM pictures showing the primary shear zone in an AISI 1040 Steel grade machined at a cutting speed of 73 m/min. There is no evidence of void nucleation in the pearlite colony, though the lamellae exhibit severe local deformation. However, each of the elongated inclusions are clearly seen to be associated with a large cavity, the length of the cavity being well over twice the length of the elongated inclusion. At still higher cutting speeds i.e. at 110 m/min., the AISI 1040 grade steel shows evidence of serrated chip formation, see Figure B8.

At still higher speeds, discontinuous chip formation results and the type of chip obtained from machining CK45 material at 200 m/min. is shown in Figure B9. The chemistry of CK45 material is given below.

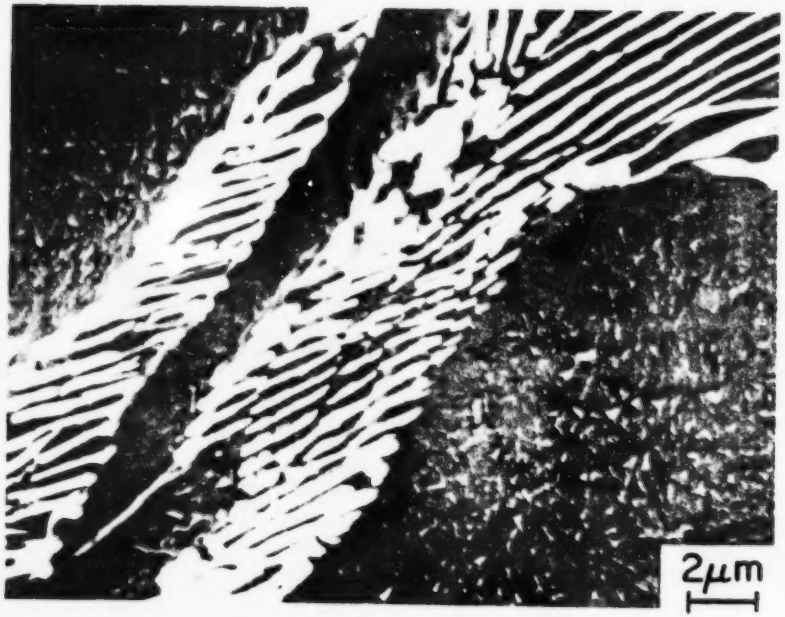

Figure B4:

Lamellar pearlite oriented at an angle to the tensile axis in the primary shear zone.
Steel Grade 1018 V = 73 m/min

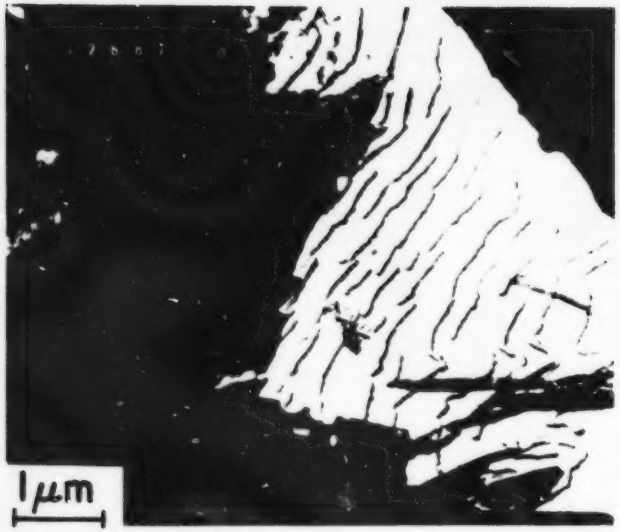

Figure B5:

TEM picture of a replica extracted from the primary shear zone of a quick-stop chip ; lamellar pearlite oriented parallel to the tensile axis.
Steel Grade 1018 V = 110m/min

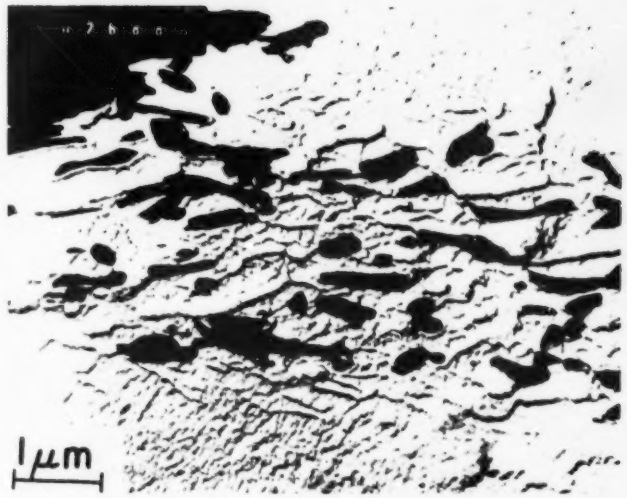

Figure B6:

TEM picture of a replica extracted from the primary shear zone ; lamellar pearlite oriented transverse to the tensile axis.
Steel Grade 1018 V=110 m/min

Figure B7:

Section through primary shear zone of a chip after quick-stop.
Steel Grade 1040 V = 73 m/min
Note extended void growth around inclusions.

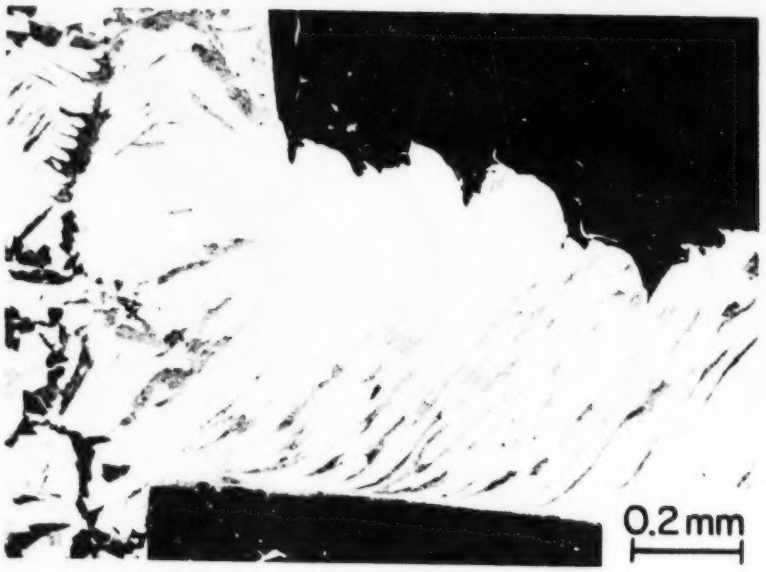

Figure B8:

Section through chip after quick-stop showing serrations
Steel Grade 1040 V=110 m/min

Figure B9:

CK 45 Shear - localised chip
V = 200 m/min

Figure B10:

CK 45 Shear - localised chip
V = 200 m/min

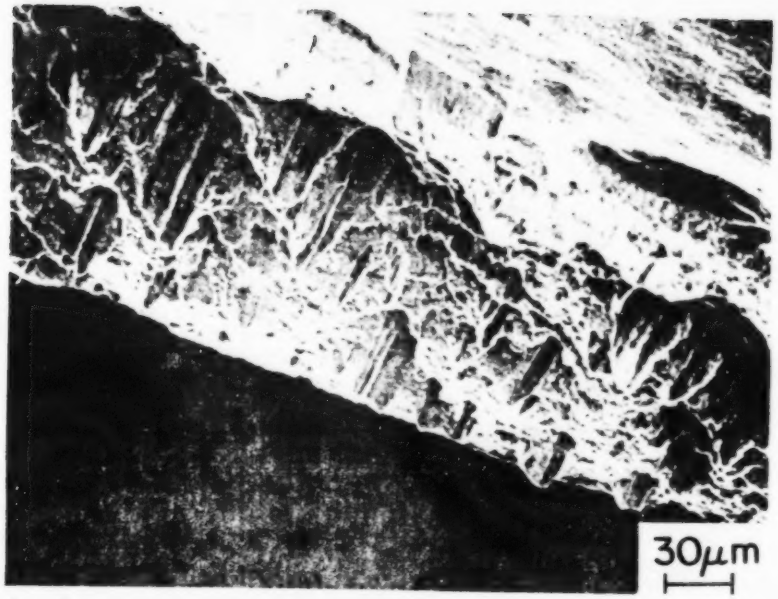

(a)

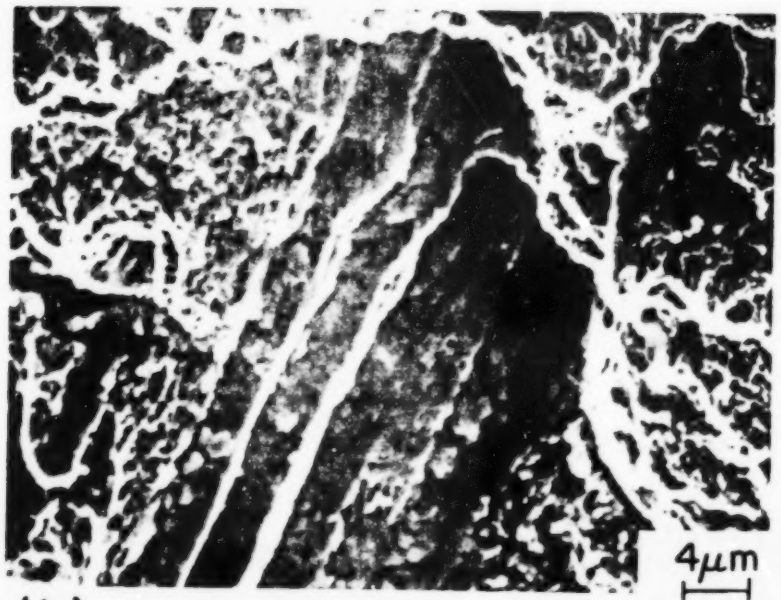

(b)

Figure B11:

CK 45 V = 200 m/min
Voids around inclusions in ductile rupture zone.

Material	C	Si	Mn	P	S
CK45-1	0.45	0.20	0.77	0 009	0.035
CK45-2	0.45	0.20	0.77	0.009	0.056

An SEM picture of this chip, given in Figure B10 shows evidence of segmentation. A detailed examination of the fracture surface under the SEM showed two distinct regions. There is a region of ductile rupture, with characteristic dimples, as shown in Figure B11(a). Inclusions in this region are associated with very extensive void growth and linkage, Figure B11(b). The other region shown in Figure B10 and B11(a) corresponds to the segmented fracture surface of the chip, which is smooth and undeformed. Thus, following the region of ductile rupture, there appears to be a region of catastrophic crack propagation. However, the segmentation of the chip is incomplete at the cutting speed of 200 m/min. The effect of increasing the sulfur content from 0.035 to 0.056 wt, did not appear to influence the degree of segmentation significantly.

Figure B12 shows typical chips obtained at 2000 m/min. in CK 45 material. The SEM picture of the chip, given in Figure B13, clearly shows that the chip is highly segmented. Figure 14(a) shows the ductile and shear localised regions of the chip. Figure 14(b) shows voids around the inclusions in the ductile rupture zone, the stage prior to the coalescence of voids into the crack.

B3 DISCUSSION

B3.1 Ductile Fracture of Chips

A basic understanding of fracture processes associated with chip formation in metal cutting is essential in order to improve the machinability of a given steel grade for a given rate of metal removal. The deformation process associated with chip formation in metal cutting is a heterogeneous one, involving high strain rates ($\dot{\varepsilon} \simeq 10^4 - 10^6$/sec.) and large

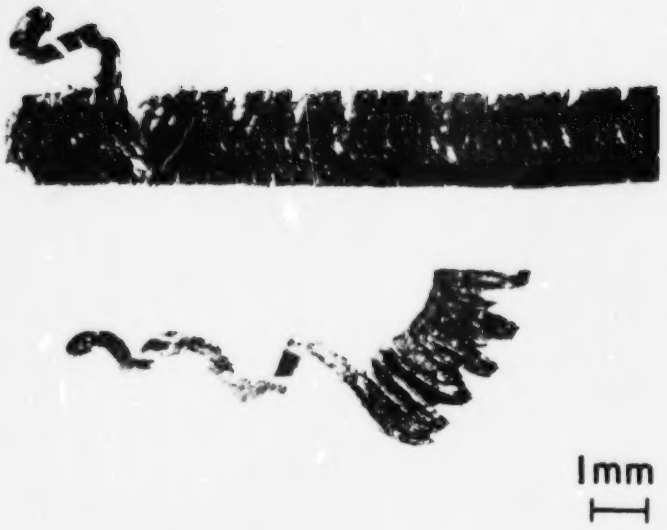

Figure B12:

CK 45 Shear - localised chip
V = 2000 m/min

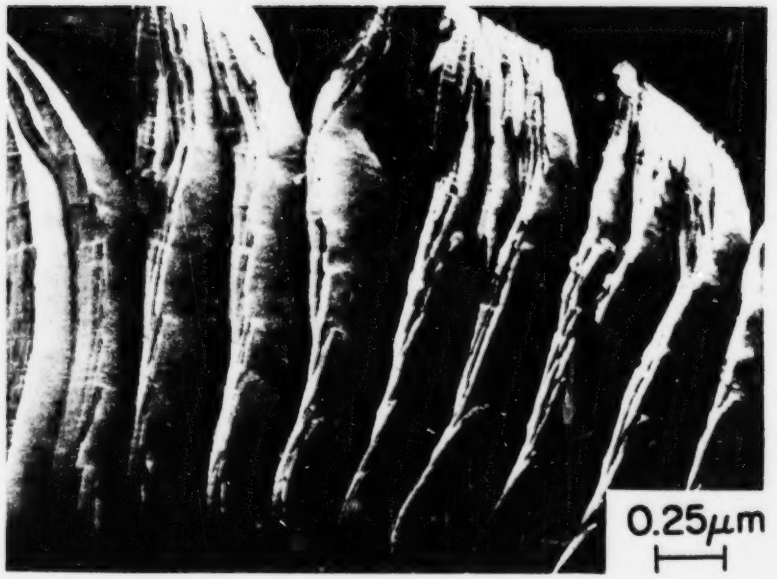

Figure B13:

CK 45 Shear - localised chip
V = 2000 m/min

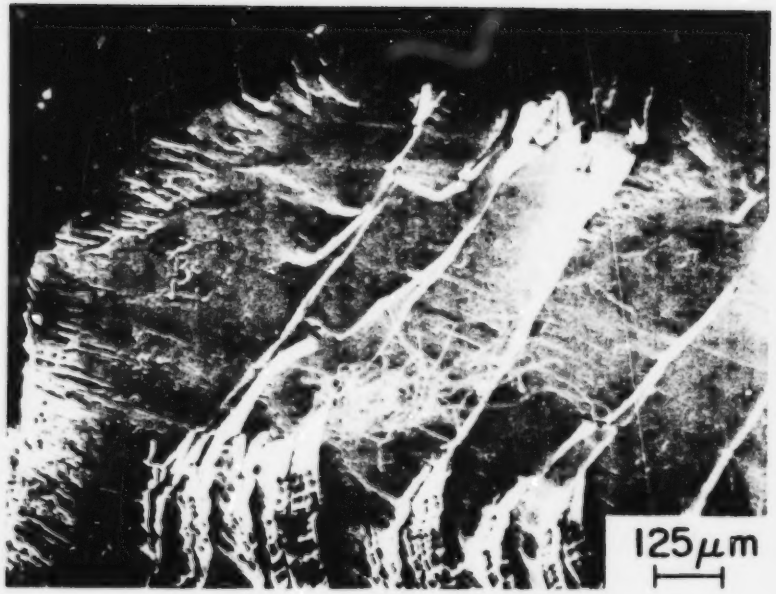

Figure B14(a)

Ductile and shear zones of fracture in the shear-localised chip

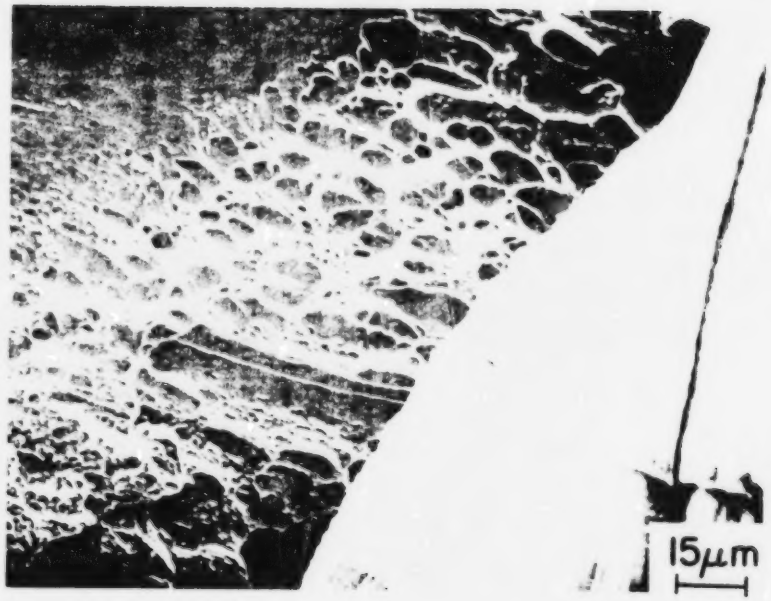

Figure B14(b)

Voids around inclusions in ductile rupture zone
CK45 V= 2000 m/min

strains ($\varepsilon > 1$) in a highly localised zone of a few microns in thickness in the workpiece, extending from the tool/work contact. The detailed examination of the quick-stop sections of low and medium carbon steels at moderate cutting speeds (70 m/min. and 110 m/min.), shown in Figures B1 and B8 clearly shows that the fracture starts off in a ductile mode in the primary shear zone. Even at higher cutting speeds of 200 m/min. and 2000 m/min., the ductile rupture regions are clearly seen, Figures B11(a), B11(b), B14(a) and B14(b). However, at higher speeds, approaching 2000 m/min., the coalescence of voids into cracks has culminated in fracture processes leading to chip segmentation, Figures B12 and B13.

The various stages leading to a total failure due to ductile fracture may be summarised as follows:

i) As the material is progressively worked, second phase particles and interphase interfaces start acting as centres for the formation of voids. Void initiation occurs because of the inherent deformation incompatabilities which exist between the second phase particles and the surrounding matrix.

ii) Increasing plastic strain promotes void growth.

iii) As deformation damage accumulates, microstructural instability occurs resulting in void coalescence.

The process of damage accumulation occurs concomitantly with the process of strain hardening, leading to final failure. All the three stages of void nucleation, growth and linkage are in competition with general and localised plastic flow events. Thus, the damage accumulation will depend upon the flow stress level, the state of stress and the microstructural parameters which govern the alternative flow and fracture modes. The results of the present investigation based on SEM studies of quick stop samples and chips can be analysed to examine (a) the influence of the orientation and the volume fraction of sulfide inclusions and pearlite at moderate cutting speeds on the damage accumulation process, and (b) the effect of cutting speed on the chip fracture processes in a medium carbon steel.

B3.2 Damage at Moderate Cutting Velocities

B3.2.1 Void Nucleation Void nucleation is associated with the fragmentation of cementite particles in a low carbon steel as shown in Figure B1(b). In contrast, MnS inclusions oriented parallel to the tensile axis in the primary shear zone are intact and voids are confined to the tips of the elongated MnS inclusions, Figure B2.

There is an increasing incidence of carbide cracking with decreasing angle of fibre orientation to the tensile axis. The fracture in the carbides is not randomly oriented but tends to be concentrated in the middle of the cementite plates along their length. These observations tend to support a model of particle fracture based upon a fibre loading mechanism rather than a blocked slip or dislocation pile-up mechanism. A pile-up mechanism would predict a random distribution of cracks with respect to both their angular orientation to the tensile axis and their position along the carbide length. Fibre loading assumes that the tangential forces exerted on the particle surface by the yielding matrix are balanced by a tension in the non-deforming particle (1-3). The total force exerted on the particle increases with distance from the particle end and so the maximum stress within the particle occurs at its centre. Since the stress level is dependent upon the macroscopic plastic strain, those particles whose major axes lie closest to the tensile axis will fracture preferentially. In the case of MnS, cavities are formed by interfacial separation at the tips of the elongated inclusions; this implies that the cohesive energy of the MnS/matrix interface is low. Further, as the MnS fibre is less stiff than Fe_3C (i.e. $E_{MnS} < E_{Fe_3C}$), the load sharing for the MnS case will be such as to favour an increase in maximum shear stress in the matrix in relation to the maximum tensile stress in the fibre.

The effect of fibre orientation with respect to the tensile axis is to reduce the tensile stress required to failure. Failure could occur by fracture of the fibres under tensile loading, or by shear of the matrix parallel to the fibres, or by flow of the matrix transverse to the fibres. The failure modes are competitive and failure will be determined by the one that requires the least local applied stress. Thus, there is evidence of MnS fragmentation, as

shown in Figure B1(b), where the inclusion is oriented at an angle to the tensile axis. There is also evidence of decohesion around MnS inclusions in the secondary shear zone, as can be seen in Figure B3. However, all the MnS inclusions in the bar stock are oriented parallel to the general rolling direction. Thus, the local orientation differences of MnS inclusions occurring in the primary and secondary shear zones are a direct consequence of general and local plastic flow during chip formation. As the volume fraction of pearlite is increased to 22.5% ($V_{Fe_3C} \simeq$ 3%) in a 1018 Grade steel, failure occurs by shear at an angle to the fibres, see Figures B4 and B6. With further increase in the volume fraction of pearlite to 50% ($V_{Fe_3C} \simeq 6\%$) in a 1040 Grade steel, the structure consists of pearlite colonies with a fine interlamellar spacing, and ferrite. The fine carbide lamellae are able to bend or deform in contrast with the coarser carbide lamellae obtained in the low carbon steels which cracked and initiated void nucleation. Increasing pearlite content increases the flow stress at any given strain and also increases the work-hardening rate (4). Under these conditions, the stress level for MnS inclusion/matrix decohesion is readily reached; as the plastic deformation is localised in ferrite, extensive void growth is observed, see Figure B7.

In low carbon steel, coarser carbides can crack and initiate ductile fracture. Void nucleation associated with the fragmentation of cementite particles contributes significantly to the damage process. Thus MnS inclusions appear to play a less important role in the nucleation of voids in the low carbon steels (C < 0.18%). On the other hand, in medium carbon steel, where the structure consists of fine pearlite colonies and ferrite, void nucleation occurs by decohesion of MnS/matrix interfaces. Thus the MnS inclusions are effective in contributing to the damage process that results in the fracture of chips.

It is important to analyse the damage accumulation process during chip formation by identifying the microstructural parameters that contribute to void nucleation. The relationship between the nucleation strain and stress state can be determined by considering all of the stress terms contributing to particle-matrix decohesion. These stresses can be defined as (i) the flow stress, σ_f, which acts to open up a void parallel to the tensile axis, (ii) the

local stress, σ_c that arises from the incomplete plastic relaxation around the particle (5), and (iii) any hydrostatic stress, σ_H that may be applied (2). Cavity nucleation occurs when the sum of the stresses is greater than the strength of the particle-matrix interface, σ_I, i.e., the stress at which decohesion occurs.

According to Goods and Brown (2), the condition for void nucleation is:

$$\sigma_c + \sigma_f + \sigma_H > \sigma_I;$$

and the critical strain, ϵ_c, to nucleate a void is

$$\epsilon_c \geq 1.7 \cdot \frac{r}{b}\left(\frac{\sigma_I - \sigma_H - 3\sigma_o}{\mu}\right)^2\left(1 + 3f_v + \frac{f_v^{1/2}}{1.8}\right)^{-2}.$$

where

r is the particle radius,

b Burgers vector

f_v the volume fraction of particles

μ the shear modulus

and σ_o the Orowan Stress

Although it is convenient to consider an average macroscopic strain at which nucleation occurs, the nucleation event depends on local conditions. According to Embury (6), nucleation is a process which spreads through the particle distribution over a range of plastic strain. He has considered two extreme cases (a) the situation where the nucleation strain reflects the average volume fraction of particles, and (b) a condition where nucleation is dominated by the extreme values of particle distribution, such as local aggregates of inclusions.

In materials which contain a high volume fraction of second phase particles, the nucleation strain decreases linearly with the volume percentage of the second phase particles. Under these conditions the nucleation itself can be viewed not as a unique event but as a cumulative damage event, in which the process of decohesion spreads through the existing particle dispersion. More recently, Chandrasekaran and Sowerby (7) have modified

McClintock's model for void growth. In their work, the nucleation is considered as a continuous process, which is probably a more realistic situation. Further work is required to examine the influence of the aspect ratio, the orientation with respect to the tensile axis, nonuniformity in the local distribution of second phase particles on void nucleation. The recovery associated with the temperature effects have to be examined in the context of machinability.

B3.2.2 Void Growth: The process of growth has been considered by different authors using continuum models. The problem is one of dealing with the rate of change of the radii of an isolated void in an imposed strain rate field. The elegant solutions developed by Rice and Tracy (8) and McClintock (9) have predictive capability. This approach has been successfully used to describe the void growth behaviour of an isolated void embedded in a strain hardening matrix (10). The models can be used to describe interparticle void growth under a given state of stress.

B3.2.3 Void Coalescence: Void coalescence is a catastrophic event, which does not contribute to any increase in plastic strain. The voids expand and at some stage in their growth become unstable and the link up of adjacent cavities takes place in a catastrophic fashion.

B3.3 Non-Uniform Void Dispersion:

The problem of plastic flow localisation due to non-uniform void distribution has been analysed by Ohno and Hutchinson (11). A model is proposed for an elastic-plastic solid with an excess of voids in a disk-shaped cluster embedded in a uniform background distribution. The model is used to study the effect of the void cluster on the plastic flow localisation. The study unambiguously indicates that small clusters are not deleterious at low triaxialities of stress but are deleterious at high triaxialities. The model considers bands oriented perpendicular to the direction of maximum principal strain. Band orientations oblique to this

orientation are expected to be more critical in the range of low triaxialities. This is an excellent approach and requires to be followed up in order to elucidate the influence of nonuniform distribution of second phase particles on the micromechanisms of ductile fracture processes involved in chip formation over a range of cutting speeds.

At moderate cutting speeds, continuous chips result. This would imply that the rate of damage accumulation is inadequate to culminate in a fracture event.

B3.4 The Effect of Cutting Velocity

In a medium carbon steel, the effect of increasing the cutting speed is to promote the chip fracture process. At a low cutting speed of 73 m/min., continuous chips are obtained, however, the chips obtained from a 1040 Grade steel at 110 m/min. show evidence of serrations, see Figure B8. At 200 m/min., the chips from a CK45 Grade steel (C = 0.45% C) exhibit signs of segmentation, though the chips are of the continuous type, see Figures B9 and B10. The chips in this transition regime exhibit a ductile rupture region, followed by a fracture surface in a region devoid of any deformation. At 2000 m/min., the chips from CK45 material are almost completely segmented, see Figures B12 and B13. Thus there is a transition in the chip formation process, whereby the continuous ribbon-like chip appears at low and moderate cutting speeds and at high speeds the chip becomes segmental. There seems to be a region in the speed domain in which the transition takes place, beginning with serrated edges and progressing through an increasing degree of segmentation. The speed domain in which the transition takes place can be lowered by previous cold working of the work piece (12). This is consistent with the concept of critical cumulative damage for the onset of fracture. The chips exhibit a ductile rupture region followed by a fracture surface in a region that has undergone little deformation, see Figure B14(a). The ductile rupture region in Figure B14(b) clearly shows evidence of cavitation associated with the MnS inclusions. The dimples are associated with fine carbide particles. The void coalescence is complete in

many cases. Thus there is strong metallurgical evidence to support strain localisation during chip segmentation.

It is not known how the temperature is affected by the cutting speed. At higher temperatures, when dislocation mobility by climb is high, plastic relaxation is easy and local work-hardening is small (2). Thus the cavity nucleation will be rendered difficult at higher temperatures. In view of the fact that the continuous chip is a nuisance in automatic operations, and that a considerable increase in productivity is to be gained by moving to higher speeds, there is much technological interest in higher cutting speeds. A major question is such work is whether or not adiabatic heating can lead to dynamic recovery or even localised melting in the shear zones of cutting.

The temperature in the primary zone for a continuous chip is calculated as a function of cutting speed for an AISI 1045 Grade steel by Wright and Bagchi (13); the temperature increases from 400°C at 300 m/min. to 500°C at 2400 m/min. Following Wright and Robinson (14), the following constitutive equation could be written:

$$\tau(T, \gamma, \dot{\gamma}) = \tau_y (T_o, \gamma_y, \dot{\gamma}_y) + \frac{\partial \gamma}{\partial T} \Delta T + \frac{\partial \tau}{\partial \gamma} \Delta \gamma + \frac{\partial \tau}{\partial \dot{\gamma}} \cdot \Delta \dot{\gamma} + \frac{\partial \tau}{\partial \theta} \cdot \Delta \theta$$

where

τ is the flow stress at any temperature T,

γ the strain

$\dot{\gamma}$ the strain rate in the primary shear zone

τ_y the shear yield stress at the yield strain γ_y, yield strain rate γ_y and starting temperature T_o

At shear strain rates $\dot{\gamma} \simeq 10^4 s^{-1}$, the rate of dislocation movement is partly controlled by phonon and electron damping mechanisms so that the yield strength increases rapidly with strain rate. The material is further deformed after yielding, and very high values of shear strain, typically $\gamma = 2$–5, occur. This intense strain hardening is expected to occur together with the dislocation damping mechanism on account of the high strain rate. At the same time

the plastic work done on the material causes a considerable heat input. These factors offset one another to some extent but softening is time dependent. Since softening is thermally activated,

$$\frac{\partial \tau}{\partial \theta} = -K \exp\left(-\frac{Q}{RT}\right),$$

where Q is the molar activation energy.

An element typically spends about 200 μs in the primary shear zone, which is not enough to soften the material significantly. At ultra high speeds, there is evidence for catastrophic shear in chips consisting of narrow bands (0.002 mm) separated by much larger regions that exhibit little strain. Physically such segmental chips resemble the discontinuous chip type.

The occurrence of modest adiabatic shear effects in the primary zone should be expected to lead to a small or negative value for the strain hardening exponent n, in the stress strain relationship

$$\sigma = \sigma_1 (\epsilon)^n$$

where σ and ϵ are the equivalent stress and strain, and σ_1 the stress at a strain $\epsilon = 1$. Using Kececioghi's data (15), Wright and Robinson (14) obtain negative n orders to support the argument that adiabatic shear does indeed occur in the primary shear zone of continuous chip formation.

In the secondary shear zone, even though strain rates are not as high as in the primary shear zone, the strains are much greater, $\gamma_s = 20 - 100$. When machining low carbon steel, the estimated temperatures are of the order of 1000°C, illustrating that the ratio of heat energy generated to heat lost is small. Thus the opportunity for dynamic hot-working is much greater in the secondary shear zone than in the primary zone. Under these conditions, the structure obtained in quick-stop samples will be affected by transformation and static recrystallisation following the arrest. Thus, the interpretation of the results from quick stop sections is rendered difficult.

B3.5 Conclusions

I. Chip Formation in Medium Carbon Steels (0.4% C)

I.1 The chips obtained from a medium carbon steel change from a continuous chip at a low speed of 70 m/min. to a serrated chip at 110 m/min.; at a higher speed of 200 m/min., the chip exhibits a low degree of segmentation but at 2000 m/min. the chip is nearly completely segmented.

I.2 In the continuous chip formed in a medium carbon steel, there is evidence of void nucleation and growth associated with MnS inclusions in the primary shear zone. Void nucleation is associated with decohesion at the inclusion/matrix interface, a feature that is observed in the secondary shear zone as well.

I.3 As the cutting speed is increased, there is evidence of plastic flow in the pearlite colonies occurring in the primary shear zone; however extended cavity growth occurs on account of plastic flow localisation. Coalescence of cavities leads to the serrations on the chip surface furthest from the rake face.

I.4 At 200 m/min., the medium carbon steel exhibits a moderate degree of segmentation. The chips exhibit a well defined ductile rupture region with characteristic dimples followed by a fracture surface devoid of dimples. Extensive cavity growth can be identified with each MnS inclusion.

I.5 At 2000 m/min., the medium carbon steel chips exhibit complete segmentation; the segments show a ductile rupture region with chracteristic dimples, followed by a fracture surface devoid of dimples. Extensive cavity growth around MnS inclusions occurs. Thus, MnS inclusions contribute to the formation of cavities which eventually grow and coalesce into a crack and result in the fracture of the chips.

II. Chip Formation in Low Carbon Steels (< 0.18)

II.1 In very low carbon steels, (i.e. C < 0.1 w%), there is evidence of void nucleation associated with the cementite fibres. If elongated MnS inclusions and cementite fibres are oriented parallel to the tensile axis in the primary shear zone, the mechanism of fibre loading of the stiffer cementite plates possibly operates, leading to the observed fragmentation of the carbide fibre; voids preferentially nucleate at the fragmented carbide/matrix interface. However, the void nucleation in the case of MnS is confined to the tips of the elongated inclusion.

II.2 The orientations of the MnS inclusions are different from those in the uncut workpiece and are influenced by the macroscopic flow, but the void nucleation for a given orientation in the primary and secondary shear zones is dependent upon the state of stress existing locally.

II.3 Void nucleation in a low carbon steel is influenced by the fibre-loading mechanism and hence by the aspect ratio and orientation of fibres. The elastic and shear moduli of the second phase particles have to be considered in a detailed numerical analysis, to elucidate the role of free cutting additives in a low carbon steel grade.

II.4 The damage processes leading to the fracture of chips are influenced by the pearlite as well as the MnS inclusions in the low carbon steel. Unlike the medium carbon steel, the role of free cutting additives in promoting ductile fracture is less well defined in the case of low carbon steels because of the competing mechanisms of damage processes, i.e., fibre loading and dislocation pile-up mechanisms.

B4. FUTURE WORK

A detailed modelling of chip formation has to consider:

a) the macroscopic flow of the material under the given machining conditions and material parameters and

b) the microscopic criteria involving damage accumulation processes due to strain localization.

The stress distributions in the primary and secondary shear zones of the chip will be analysed on continuum mechanical principles using numerical techniques. The deformation behaviour of the material in the primary and secondary shear zones will be influenced by strain, strain rate and temperature distribution, all of which have to be taken into consideration in the analysis of macroscopic plastic flow.

The effect of microstructural parameters such as the size, shape, aspect ratio and orientation of the second phase particles on strain localization, and thus on void nucleation, can be analysed using the criterion for void nucleation given by Goods and Brown (2). The concept is that cavity nucleation occurs when the sum of the stresses arising from the flow stress, the local stress and the hydrostatic stress exceeds the strength of the particle-matrix interface or the particle strength.

Void growth can be analysed using McClintock's model, as modified by Chandrasekasan and Sowerby (7), to take into account the continuous nucleation process. The influence of non-uniformity in the local dispersion of voids on void growth has to be considered. The concept of critical accumulated damage to fracture will have to used to analyse the chip formation process.

The effect of temperature and microstructural properties, such as particle/matrix interfacial strength, the elastic and shear moduli of the particle and the matrix, on the fracture processes can be studied using the model. A basic understanding of the fracture processses underlying chip formation is the key to the design of the optimum microstructure for the improved machinability of the steel.

SECTION B - REFERENCES

1. A. Kelly, Proc. R. Soc. (A), 282, 63 (1964)
2. Goods and Brown, Overview No. 1, Acta Met., V.27, p. 1-15, (1979).
3. A. Kelly, 'Strong Solids', Clarendon Press, Oxford, (1966), p. 127.
4. T. Gladman, B. Homes and F.B. Pickering, J. Iron Steel Inst., (1970), 208, p. 172.
5. L.M. Brown and W.M. Stobbs, Phil. Mag., 34, 351 (1976).
6. J.D. Embury, Proc. Of Int. Conf. on 'Strength of Metals and Alloys', Melbourne, Australia (1982).
7. N. Chandrasekaran and R. Sowerby, to be published.
8. J.R. rice and D.M. Tracy, J. Mech. Phys. Solids, (1969), 17, p. 201.
9. F.A. McClintock, 'Ductility' ASM Publication (1968), p. 255.
10. N. Chandrasekaran and R. Sowerby, Private Communication.
11. N. Ohno and J.W. Hutchinson, J. Mech. Phys. Solids, Vol. 32, No. 1, pp. 63-85, 1984.
12. B.F. von Turkovich, Annals of the CIRP, Vol. 32, No. 2, 1983, p. 609.
13. P.K. Wright and A Bagchi, Manufacturing Engineering Trans., (1980), p. 277-284.
14. P.K. Wright and J.L. Robinson, J. of Metals Technology, (1977) Vol. 4. p. 240.
15. D. Kececiouglu, Trans ASME, (1958), V. 80, p. 158.

ACKNOWLEDGEMENTS

Helpful discussions with Prof. J. D. Embury and Mr. N. Chandrasekaran are gratefully acknowledged. The high speed chips used in this investigation were provided by the research group headed by Prof. Tönshoff at IFW, the University of Hanover, and the low speed quick stop samples were provided by Prof. Tlusty before he moved to the University of Florida. Special thanks are expressed to them. The assistance of Mrs. Teresa Castillo with the SEM work is gratefully acknowledged.